




## Entanglement dynamics in the many-body Hatano-Nelson model

Takahiro Orito 

Graduate School of Advanced Science and Engineering, Hiroshima University, Higashi-Hiroshima 739-8530, Japan  
Institute for Solid State Physics, The University of Tokyo, 5-1-5 Kashiwanoha, Kashiwa 277-8581, Japan

Ken-Ichiro Imura 

Institute of Industrial Science, The University of Tokyo, 5-1-5 Kashiwanoha, Kashiwa 277-8574, Japan

 (Received 9 August 2023; revised 25 October 2023; accepted 17 November 2023; published 13 December 2023)

The entanglement dynamics in a non-Hermitian quantum system is studied numerically and analyzed from the viewpoint of quasiparticle picture. As a concrete model, we consider a one-dimensional tight-binding model with asymmetric hopping (Hatano-Nelson model) under onsite disorder and nearest-neighbor interaction. As opposed to an assertion of previous studies, the entanglement dynamics in this non-Hermitian quantum system is very different from the one in its Hermitian counterpart, especially in the delocalized regime with weak disorder; there the entanglement entropy  $S_{\text{ent}}(t)$  shows a characteristic nonmonotonic time evolution. We have clarified and quantified the nature of this behavior in the quasiparticle picture. In the asymptotic regime of  $t \rightarrow \infty$ , the entanglement entropy  $S_{\text{ent}}(t)$  in this regime saturates to a much suppressed value, which increases only logarithmically with respect to the size of the subsystem.

DOI: [10.1103/PhysRevB.108.214308](https://doi.org/10.1103/PhysRevB.108.214308)

### I. INTRODUCTION

The entanglement entropy  $S_{\text{ent}}$  quantifies nonlocal correlation between quasiparticles in a many-body quantum state, such as the one in an EPR (Einstein-Podolsky-Rosen) pair [1–6]. In the process of quantum thermalization [7–9] or relaxation [10–13], the so-called quasiparticle picture [14–18] (Fig. 1) makes this point explicit. A pair of entangled quasiparticles generated at  $t = 0$  move apart, and as time passes by, they are more likely found in a different subsystem [see Fig. 1(a)]. This leads to an increase of the entanglement entropy  $S_{\text{ent}}$  [cf. its bipartite definition, Eq. (18)]. Correspondingly, the reduced density matrix of the subsystem becomes a *mixed* state [cf. Eq. (19)] [19,20].

In a system in which this quasiparticle picture is well applicable, the entanglement entropy  $S_{\text{ent}}$  is an extensive quantity, obeying the volume law [21]:  $S_{\text{ent}} \propto V = L^d$  ( $L$ : size,  $d$ : dimension of the system); and indeed serves a *thermodynamic* quantity, while there are cases in which  $S_{\text{ent}}$  obeys the area-law scaling  $S_{\text{ent}} \propto V = L^{d-1}$ . The latter includes the cases of nonunitary time evolution induced by dissipation [22], projective measurements [23,24], and also some parameter regime of a  $PT$ -symmetric system [25,26]. If one can manipulate a parameter of the system to drive the system from one case to the other, the entanglement entropy  $S_{\text{ent}}$  is subject to a transition from volume- to area-law scaling [23]. This transition, dubbed as the entanglement transition, has been attracting much attention recently, in theoretical [27–33], experimental [34,35], and numerical contexts [36–38].

We consider, as a concrete example, the case of a many-body Hatano-Nelson (HN) model [39–41]: a one-dimensional tight-binding model with asymmetric (nonreciprocal)

hopping, which is specified by a parameter  $g$ . In dynamics, due to the asymmetry in hopping, an initial wave packet does not spread as in the Hermitian case, but rather slides in the direction specified by the asymmetry of hopping (sign of  $g$ ) [42]. Such a unidirectional motion is robust against disorder and suppresses wave packet spreading [43]. This peculiar wave-packet dynamics leads to a remarkable nonmonotonic time evolution of the entanglement entropy  $S_{\text{ent}}(t)$  [44]. In the body of the paper, we provide an intuitive explanation on the increase of  $S_{\text{ent}}$  in the delocalized regime from the viewpoint of the quasiparticle picture.

This work is also an outcome of a technical advancement we have made in our numerics. Here, we have successfully employed the Krylov subspace method [45] in our problem, which has allowed us to deal with a system of larger size than the previous studies, e.g., the one of our own [44]. This has been particularly helpful in the study of the scaling property of  $S_{\text{ent}}$ .

The paper is organized as follows. In Sec. II, we introduce the HN model, the numerical conditions, and the definition of entanglement entropy. In Sec. III, we systematically investigate the effect of disorder on the density dynamics in the real and momentum spaces and entanglement dynamics. In Sec. IV, we point out the difference in the entanglement dynamics between the non-Hermitian and Hermitian systems in the clean limit from the perspective of the quasiparticle picture. In Sec. V, we investigate whether non-Hermiticity induces entanglement transition. In Sec. VI, we examine various aspects of  $S_{\text{ent}}$ , such as its scaling behavior, the effect of interaction, and its relation to the correlation function. Section VII is devoted to concluding remarks. Some details are left in the Appendixes and Supplemental Material [43].

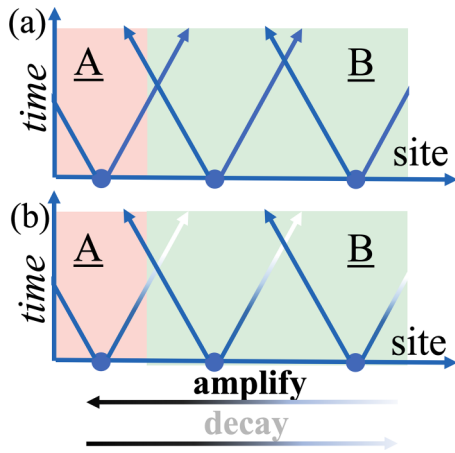


FIG. 1. Schematic illustration of the quasiparticle picture: (a) in the Hermitian case, and (b) in the case of the Hatano-Nelson-type asymmetric hopping model (non-Hermitian case).

## II. MANY-BODY HATANO-NELSON MODEL

Let us first introduce our model, which is a many-body extension of the so-called Hatano-Nelson (HN) model [39–41] and reads as in the second quantization representation

$$\mathcal{H} = - \sum_{j=0}^{L-1} (\Gamma_L c_j^\dagger c_{j+1} + \Gamma_R c_{j+1}^\dagger c_j) + \sum_{j=0}^{L-1} (V \hat{n}_j \hat{n}_{j+1} + W_j \hat{n}_j), \quad (1)$$

where  $c_j^\dagger$  ( $c_j$ ) is a fermionic creation (annihilation) operator of a particle at site  $j$ , while  $\hat{n}_j = c_j^\dagger c_j$  is a number operator which counts the number  $n_j$  of such particles found at site  $j$ . Here, we choose the boundary conditions to be periodic, i.e.,  $c_L = c_0$  and  $c_L^\dagger = c_0^\dagger$ . The first two-terms represent the asymmetric hopping, where the degree of nonreciprocity (asymmetry) is specified by the parameter  $g$ :

$$\Gamma_L = e^g \Gamma_0, \quad \Gamma_R = e^{-g} \Gamma_0. \quad (2)$$

In the third term,  $V$  represents the strength of the nearest-neighbor interparticle interaction, while in the last term,  $W_j$  represents the depth of an onsite disorder potential at a site  $j$ . Here, unlike in the original Hatano-Nelson model [39–41], in which the random numbers  $W_j$ 's obey to a uniform distribution, we consider the case in which  $W_j$  represents a quasiperiodic potential (cf. the Aubry-André model [46]):

$$W_j = W \cos(2\pi\alpha j + \theta), \quad (3)$$

where  $\alpha$  should be chosen to be an irrational number, e.g.,  $\alpha = (\sqrt{5} - 1)/2$ . For  $\alpha$  thus chosen, the quasiperiodic potential  $W_j$  mimics a random/disorder potential as the one in the original Hatano-Nelson model,  $W$  represents the strength of the disorder potential. If an average over different disorder configurations is necessary, one can activate the parameter  $\theta$  in Eq. (3), and take the average over  $\theta$ .

Although the original Hatano-Nelson model [case of  $V = 0$  in Eq. (1)] has first appeared [39–41] as an effective model describing the phenomenon of vortex (de)pinning, it is now considered to be a prototypical non-Hermitian situation, and

readapted in a number of different works. The aspect of asymmetric hopping  $g \neq 0$  leads (under the open boundary) to the so-called non-Hermitian skin effect, and is much discussed in the context of the idea of non-Hermitian topological insulator [47–58]. The competition between the effect of asymmetric hopping  $g \neq 0$  and that of the disorder potential  $W \neq 0$  leads to a typical delocalization-localization transition in this non-Hermitian system, and the model is also much discussed in this context [59–65]. If the localization length  $\xi$  is known in the Hermitian limit, the localization transition is expected to occur at  $g = \xi^{-1}$  in the corresponding non-Hermitian model [39–41]. In a noninteracting system, either Hermitian or non-Hermitian,  $\xi$  can be calculated by the transfer matrix method [66–69]. In an interacting system, this is simply not possible, while the study of the interacting Hatano-Nelson model brings about some information on the many-body localization length [44,70] since the asymmetric hopping  $g$  can be interpreted (under the periodic boundary) as an imaginary flux.<sup>1</sup>

### A. Non-Hermitian many-particle dynamics

In the simulation of many-particle dynamics, we will typically consider the initial state

$$|\Psi(0)\rangle = |\Psi(t=0)\rangle = |101010\dots\rangle, \quad (4)$$

i.e., the one in the density wave form, or in the Néel form in the spin language [71]. On the right-hand side of Eq. (4), we have employed the computational basis  $|n_1 n_2 \dots n_L\rangle$ ;  $n_j = 0, 1$  represents occupation of the  $j$ th site. At time  $t = 0$ , the initial state (4) can be expressed as a superposition of eigenstates as

$$|\Psi(0)\rangle = \sum_{\alpha} c_{\alpha}(0) |\alpha\rangle, \quad (5)$$

where  $|\alpha\rangle$  represents a many-body eigenstate of the Hamiltonian (1), i.e.,  $\mathcal{H}|\alpha\rangle = E_{\alpha}|\alpha\rangle$ . Note that the eigenenergy  $E_{\alpha}$  is generally complex. In Eq. (5),  $|\alpha\rangle$  represents a right eigenstate corresponding to the eigenenergy  $E_{\alpha}$ , which is generally not identical to the Hermitian conjugate of the corresponding left eigenstate  $\langle\langle\alpha|$ , where

$$\langle\langle\alpha|\mathcal{H} = E_{\alpha}\langle\langle\alpha|, \quad (6)$$

or its conjugate

$$\mathcal{H}^{\dagger}|\alpha\rangle = E_{\alpha}^*|\alpha\rangle, \quad (7)$$

<sup>1</sup>Inserting a real flux  $\Phi$  (Hermitian system) changes a localized eigenstate  $\psi(j, \Phi = 0) \sim \exp(-\frac{|j|}{\xi})$  to  $\psi(j, \Phi \neq 0) \sim \exp(-\frac{|j|}{\xi} + i\Phi j)$ . In contrast, inserting an imaginary flux  $ig$  (HN model) modifies a localized eigenstate  $\psi(j, g = 0) \sim \exp(-\frac{|j|}{\xi})$  to

$$\begin{aligned} \psi(j, g \neq 0) &\sim \exp\left(-\frac{(1-g\xi)|j|}{\xi}\right) & \text{if } j < 0, \\ \psi(j, g \neq 0) &\sim \exp\left(-\frac{(1+g\xi)|j|}{\xi}\right) & \text{if } j \geq 0. \end{aligned}$$

One can easily observe that the delocalization transition is induced by  $ig$  and occurs at  $g = \xi^{-1}$ , from which we can determine the localization length.

or rather  $\langle\langle\alpha|\neq|\alpha\rangle^\dagger$ . To find the coefficients  $c_\alpha(0)$  in Eq. (5), one actually needs to find such left eigenstates, i.e.,

$$c_\alpha(0) = \langle\langle\alpha|\Psi(0)\rangle. \quad (8)$$

Note that the left and right eigenstates satisfy the biorthogonal condition [72]

$$\langle\langle\alpha|\beta\rangle = \delta_{\alpha,\beta}. \quad (9)$$

We then let the state (5) evolve into  $\Psi(t)$ , in principle, via the Schrödinger equation

$$i\hbar\frac{\partial}{\partial t}|\Psi(t)\rangle = H|\Psi(t)\rangle, \quad (10)$$

though, in practice, we let it evolve through a numerical recipe outlined in the next subsection. In case of a *unitary* time evolution driven by a Hermitian Hamiltonian, the weight of each eigenstate  $|\alpha\rangle$  is unchanged in the time-evolved wave packet  $|\Psi(t)\rangle$ ; if one expresses  $|\Psi(t)\rangle$  as a superposition of eigenstates as in Eq. (5), or

$$|\Psi(t)\rangle = \sum_{\alpha} c_{\alpha}(t)|\alpha\rangle, \quad (11)$$

the magnitude of the coefficients

$$c_{\alpha}(t) = c_{\alpha}(0)e^{-iE_{\alpha}t} \quad (12)$$

is conserved in the case of unitary time evolution driven by a *Hermitian* Hamiltonian, i.e., in the course of time;  $|c_{\alpha}(t)|^2$  are just constants or  $|c_{\alpha}(t)|^2 = |c_{\alpha}(0)|^2$ . Here, in the case of *nonunitary* time evolution driven by a *non-Hermitian* Hamiltonian, this is no longer the case; the coefficients  $c_{\alpha}(t)$  that appear in Eqs. (11) and (12) change constantly their amplitudes in the time evolution. In such nonunitary time evolution, the total probability  $\langle\Psi(t)|\Psi(t)\rangle$  is *a priori* not conserved<sup>2</sup> due to postselection (see Appendix A). In the actual numerical calculation, we renormalize  $|\Psi(t)\rangle$  as [42,44]

$$|\Psi(t)\rangle \rightarrow |\tilde{\Psi}(t)\rangle = \frac{|\Psi(t)\rangle}{\sqrt{\langle\Psi(t)|\Psi(t)\rangle}}. \quad (13)$$

Under this renormalization [justified physically, in Appendix A, in the context of Lindblad/GKSL (Gorini-Kossakowski-Sudarshan-Lindblad) dynamics [73,74]], the total probability is conserved, but the relative importance of  $c_{\alpha}(t)$  in Eq. (11) with respect to other  $c_{\alpha}(t)$ 's can vary. In the GKSL/quantum trajectory approach, the renormalization factor (the denominator) in Eq. (13) appears naturally as a result of the projection to null outcome; here, continuous measurement and postselection is assumed (see Appendix A for details).

Here, in the case of *non-Hermitian nonunitary* dynamics, a remarkable fact is that as time passes by, contributions from

those  $|\alpha\rangle$ 's whose eigenenergy has a large positive imaginary part become dominant in the superposition of many eigenstates  $|\alpha\rangle$  in Eq. (11); for

$$\text{Im}(E_{\alpha_1}) > \text{Im}(E_{\alpha_2}) > \dots, \quad (14)$$

$$|c_{\alpha_1}(t)|^2 \gg |c_{\alpha_2}(t)|^2 \gg \dots, \quad (15)$$

i.e., only the first few  $|\alpha_1\rangle, |\alpha_2\rangle, \dots$  become relevant in the superposition (11) if  $|\alpha_1\rangle, |\alpha_2\rangle, \dots$  are labeled in the decreasing order of  $\text{Im}(E_{\alpha})$ , and if the maximal  $\text{Im}(E_{\alpha_1})$  is sufficiently larger than the rest. If  $\text{Im}(E_{\alpha_1}) \gg \text{Im}(E_{\alpha_2})$ , in the end of the time evolution ( $t \rightarrow \infty$ ), the wave packet  $|\Psi(t)\rangle$  will be completely dominated by a single eigenstate  $|\alpha_1\rangle$ , i.e., apart from an unimportant phase factor

$$\lim_{t \rightarrow \infty} |\tilde{\Psi}(t)\rangle \sim |\alpha_1\rangle. \quad (16)$$

Thus, in the non-Hermitian quantum dynamics, the nonunitarity of the time evolution associated with the imaginary part of the eigenenergy gives rise to *collapse of the superposition* of an initial wave packet (5). After a long enough nonunitary time evolution, a generic initial state composed of many different eigenstates tends to converge to a single (or to a few) eigenstate(s).<sup>3</sup>

## B. Numerical simulation

Simulating a many-body quantum system is challenging since the size of the Hilbert space increases exponentially with the increase of size  $L$  of the system. In a simulation of a Hermitian system using the exact diagonalization method,  $L = 18$  may be a typical maximal size one can handle comfortably in a present day computer performance. In a non-Hermitian system, however, it is necessary to consider not only the eigenenergy and right eigenvector, but also the left eigenvector. Consequently, most studies are limited to treating system sizes up to  $L = 16$  [44,61,62,71,75,76]. Confronted with this numerical challenge, we have decided to employ the Krylov subspace method. In order to make it compatible with a non-Hermitian matrix, we have generated the orthonormal Krylov subspace  $V_M$  using the Arnoldi method instead of the Lanczos method [45]. The Krylov subspace is given by  $K_M = \text{span}(|\Psi(t)\rangle, H|\Psi(t)\rangle, \dots, H^{M-1}|\Psi(t)\rangle)$ . The time evolution of quantum state is described by

$$|\Psi(t + \delta t)\rangle \sim V_M e^{-i\delta t H'} V_M^\dagger |\Psi(t)\rangle = V_M e^{-i\delta t H'} |e_1\rangle, \quad (17)$$

where  $|e_1\rangle \equiv (1, 0, \dots, 0)^T$  and  $H' = V_M^\dagger H V_M$ . This allows us to calculate  $|\Psi(t + \delta t)\rangle$  by dealing with matrix  $H'$  of size  $M \times M$  instead of diagonalizing the original Hamiltonian  $H$ , and eventually enables us to study a system of larger size than those in the previous studies [44]. In the actual numerical calculations, we choose  $\delta t = 10^{-2} - 2 \times 10^{-1}$  and  $M = 10 - 25$ .

<sup>2</sup>In the Hermitian case, the total probability  $\sum_{\alpha} |c_{\alpha}(t)|^2 (= 1)$  is, of course, conserved. Here, in the non-Hermitian case, the quantity  $\sum_{\alpha} |c_{\alpha}(t)|^2$  itself does not have much meaning since  $\langle\Psi(t)|\Psi(t)\rangle \neq \sum_{\alpha} |c_{\alpha}(t)|^2$ . If one expands  $\langle\Psi(t)|$  into contributions from different *left* eigenmodes as  $\langle\Psi(t)| = \sum_{\alpha} b_{\alpha}(t)\langle\langle\alpha|$ , and uses the biorthogonal relation (9), then one finds  $\langle\Psi(t)|\Psi(t)\rangle = \sum_{\alpha} b_{\alpha}(t)c_{\alpha}(t)$ .

<sup>3</sup>Later we will encounter the case in which some largest  $\text{Im}(E_{\alpha})$ 's are quasidegenerate:  $\text{Im}(E_{\alpha_1}) \simeq \text{Im}(E_{\alpha_2}) \simeq \dots$ , and contribute equally to  $|\Psi(t \rightarrow \infty)\rangle$ . Such degeneracy in the imaginary part becomes indeed relevant in the long-time dynamics of the non-interacting case; see Secs. III and VI for details.

### C. Entanglement entropy: Definitions

In the study of many-body dynamics, we are not only interested in how the density spreads but also how correlation spreads in the system. To quantify the latter, we consider the entanglement dynamics. The entanglement entropy is a quantity to characterize the nonlocality of a quantum state, which is often defined in the sense of *bipartite* entanglement entropy:

$$S_{\text{ent}} = -\text{Tr}_A[\Omega_A \log \Omega_A], \quad (18)$$

where

$$\Omega_A = \text{Tr}_B[\Omega] \quad (19)$$

is the reduced density matrix of the subsystem A; we have divided the entire system (of size  $L$ ) into two subsystems A and B. In practice, such a division can be done using a many-body basis  $\tilde{n}$  represented by a set of quantum numbers  $\tilde{n} = \{n_1, n_2, \dots, n_L\}$ , which can be divided into the two parts as  $\tilde{n} = \{\tilde{n}_A, \tilde{n}_B\}$ , where  $\tilde{n}_A = \{n_1, n_2, \dots, n_\ell\}$  spans the subsystem A, while the remaining part  $\tilde{n}_B = \{n_{\ell+1}, n_{\ell+2}, \dots, n_L\}$  spans the subsystem B.  $\ell$  is the size of the subsystem A. In this basis, a many-body state  $|\Psi\rangle$  may be represented as

$$|\Psi\rangle = \sum_{\tilde{n}} \psi_{\tilde{n}} |\tilde{n}\rangle = \sum_{\tilde{n}_A \in A, \tilde{n}_B \in B} \psi_{\tilde{n}_A, \tilde{n}_B} |\tilde{n}_A\rangle |\tilde{n}_B\rangle. \quad (20)$$

Using this, one can explicitly trace out the subsystem B from the density matrix:

$$\Omega = |\Psi\rangle\langle\Psi| = \sum_{\tilde{n}, \tilde{n}'} \psi_{\tilde{n}} \psi_{\tilde{n}'}^* |\tilde{n}\rangle\langle\tilde{n}'|, \quad (21)$$

i.e., the reduced density matrix (19) becomes

$$\begin{aligned} \Omega_A &= \sum_{\tilde{n}'_B \in B} \langle \tilde{n}'_B | \Omega | \tilde{n}'_B \rangle \\ &= \sum_{\tilde{n}_A, \tilde{n}'_A \in A, \tilde{n}_B \in B} \psi_{\tilde{n}_A, \tilde{n}_B} \psi_{\tilde{n}'_A, \tilde{n}_B}^* |\tilde{n}_A\rangle\langle\tilde{n}'_A|. \end{aligned} \quad (22)$$

Here, we consider the time evolution of a many-body density matrix  $\Omega(t) = |\tilde{\Psi}(t)\rangle\langle\tilde{\Psi}(t)|$ , and the corresponding entanglement entropy  $S_{\text{ent}}(t)$ . Additionally, three definitions of  $S_{\text{ent}}$  (and  $\Omega$ ) arise in the context of a non-Hermitian system because the system has two eigenvectors, left and right eigenvectors. In Appendix B, we provide further explanation regarding these definitions and how they differ from one another.

### III. DENSITY AND ENTANGLEMENT DYNAMICS

In this section, we sketch the results of our numerical simulation on the (many-particle) density and entanglement dynamics. We focus on the many-body HN model with the periodic boundary condition in this study, but it is an interesting direction to study that with the open boundary condition, where the skin effect that is an intrinsic nature of the nonreciprocal hopping system appears. Based on previous studies, we comment on how a skin effect affects entanglement dynamics as well as density dynamics in Appendix C.

### A. Density dynamics in real vs reciprocal spaces

Let us first focus on the time evolution of the density profile in real space:

$$n_j(t) = \langle\Psi(t)|c_j^\dagger c_j|\Psi(t)\rangle, \quad (23)$$

where  $|\Psi(t)\rangle$  actually means  $|\tilde{\Psi}(t)\rangle$  in Eq. (13), but to simplify the notation, here, we have omitted the tilde in  $|\tilde{\Psi}(t)\rangle$ , and we will omit it hereafter. Figure 2 shows the time evolution of  $n_j(t)$  for the initial density wave (DW) pattern (4) in the non-interacting ( $V = 0$ ) [first row, panels (i-a)–(i-d)], and in the interacting ( $V = 2.0$ ) [second row, panels (ii-a)–(ii-d)] cases. In both cases the last panel [(i-d) and (ii-d)] represents the Hermitian case  $g = 0$  for comparison. Otherwise,  $g$  is chosen as  $g = 0.5$  (non-Hermitian). Different panels correspond to the varying strength of disorder:  $W = 0.5$  for panels (i-a) and (ii-a),  $W = 3.0$  for panels (i-b) and (ii-b),  $W = 5.0$  for panels (i-c), and  $W = 7.0$  for (ii-c).

In the first column [delocalized phase,  $W = 0.5$ , panels (i-a) and (ii-a)], the initial density wave pattern tends to be lost in the time evolution, while in the Hermitian case ( $V = 0$ ) [first row, panel (i-d)], the initial spatial profile does not fade but is replaced with a fast temporally oscillatory pattern<sup>4</sup> which is a feature reminiscent of an integrable system in which a perpetual motion on a regular ideal orbital is ensured by the existence of some integrals of motion (conserved quantities). In the interacting case ( $V = 2$ ) [second row, panel (ii-d)], scatterings induced by the interparticle interaction mix such regular ideal orbitals and wash out the perpetual motion. After some relaxation time  $t_1 \sim 10^0 = 1$  the spatial profile becomes *literally* uniform. The second column [panels (i-b) and (ii-b)] corresponds to the critical (crossover) regime so that the initial density wave pattern remains at least for a relatively long time. As far as these real-space features are concerned, the time evolution of the density profile  $n_j(t)$  is *not so* different from the Hermitian case [fourth column, panels (i-d) and (ii-d)]. The third column [panels (i-c) and (ii-c)] corresponds to the localized phase, where the initial density wave pattern remains over time, effectively similar to the localized phase in the Hermitian case.

Figure 3 shows time evolution of the density distribution:

$$n_k(t) = \langle\Psi(t)|c_k^\dagger c_k|\Psi(t)\rangle \quad (24)$$

in the reciprocal crystal-momentum space ( $k$  space), where

$$c_k = \sum_j c_j e^{ikj}. \quad (25)$$

As in Fig. 2, it shows the evolution of  $n_k(t)$  both in the noninteracting ( $V = 0$ ) [first row, panels (i-a)–(i-d)] and in the interacting ( $V = 2.0$ ) [second row, panels (ii-a)–(ii-d)] cases. In both cases the last panels (i-d) and (ii-d) represent the Hermitian case  $g = 0$  for comparison; otherwise,  $g = 0.5$ . Different panels correspond to the varying strength of disorder:  $W = 0.5$  for panels (i-a) and (ii-a),  $W = 3.0$  for panels

<sup>4</sup>In the thermodynamic and clean limit, the evolution of  $\langle n_j \rangle$  exhibits algebraic decay with oscillation and ultimately reaches the homogeneous state. This tendency is consistent with the feature of delocalization.



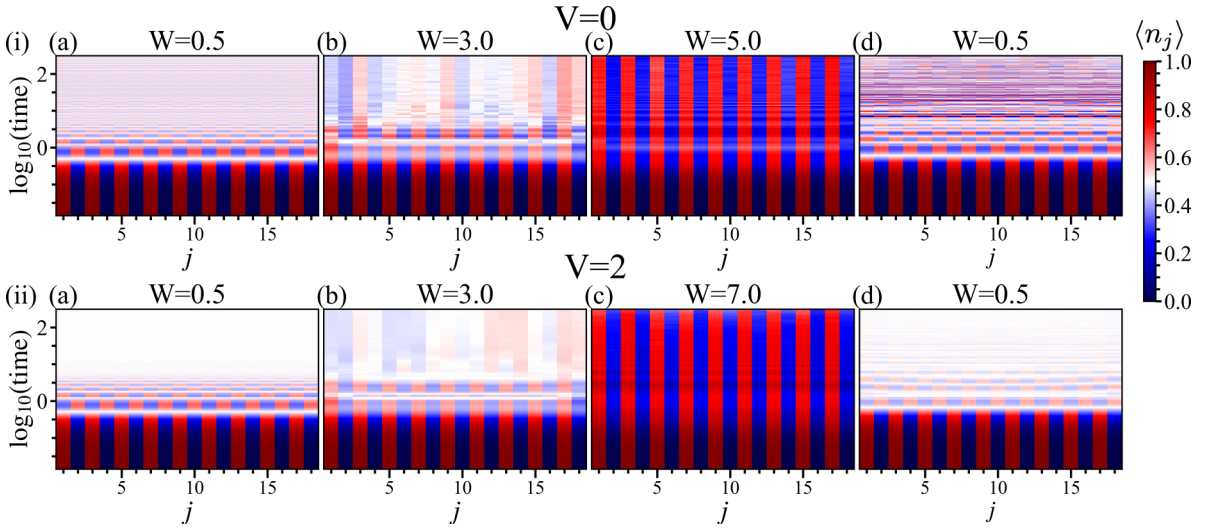


FIG. 2. Time evolution of the spatial profile of the density  $n_j(t)$ . The first row [(i-a)–(i-c)]: noninteracting case ( $V = 0$ ), asymmetric hopping ( $g = 0.5$ ), and (i-d):  $V = 0$ ,  $g = 0.0$ . The second row [(ii-a)–(ii-c)]: interacting case ( $V = 2$ ),  $g = 0.5$  and (ii-d):  $V = 2$ ,  $g = 0.0$ . In numerical calculation, for  $g \neq 0$  we carried out the evaluations with 80 (for  $V = 2$ ) and 40 (for  $V = 0$ ) samples. For the Hermitian case, we used 80 samples.

(i-b) and (ii-b),  $W = 5.0$  for panel (i-c), and  $W = 7.0$  for (ii-c).

First, unlike in the real space (Fig. 2) the time evolution of the density profile shows very different features in the Hermitian [column (d)] and non-Hermitian [especially, first two columns: (a) and (b)] cases. In these columns, one can see that as time evolves, the density distribution  $n_k(t)$  in the reciprocal space tends to converge to a certain asymptotic distribution, implying that in the regime of sufficiently long time  $t \gg 1$ , the many-body wave packet  $|\Psi(t)\rangle$  tends to approach to a single eigenstate  $|\alpha_1\rangle$  as in Eq. (16); in the noninteracting case ( $V = 0$ , e.g., in the first row of Fig. 3) and also at  $W = 0|\alpha_1\rangle$  will be given

$$|\alpha_1\rangle = \left( \prod_{k < 0} c_k^\dagger \right) |0\rangle, \quad (26)$$

implying a sharp Fermi-sea-like asymptotic density distribution  $n_k^{(\infty)} = n_k(t \rightarrow \infty)$  such that

$$n_k^{(\infty)} = \begin{cases} 1 & \text{for } k < 0, \\ 0 & \text{for } k > 0. \end{cases} \quad (27)$$

Such a density distribution  $n_k(t)$  localized in the crystal-momentum space prevails in the regime of weak disorder also in the case of weak interparticle interaction, e.g., case

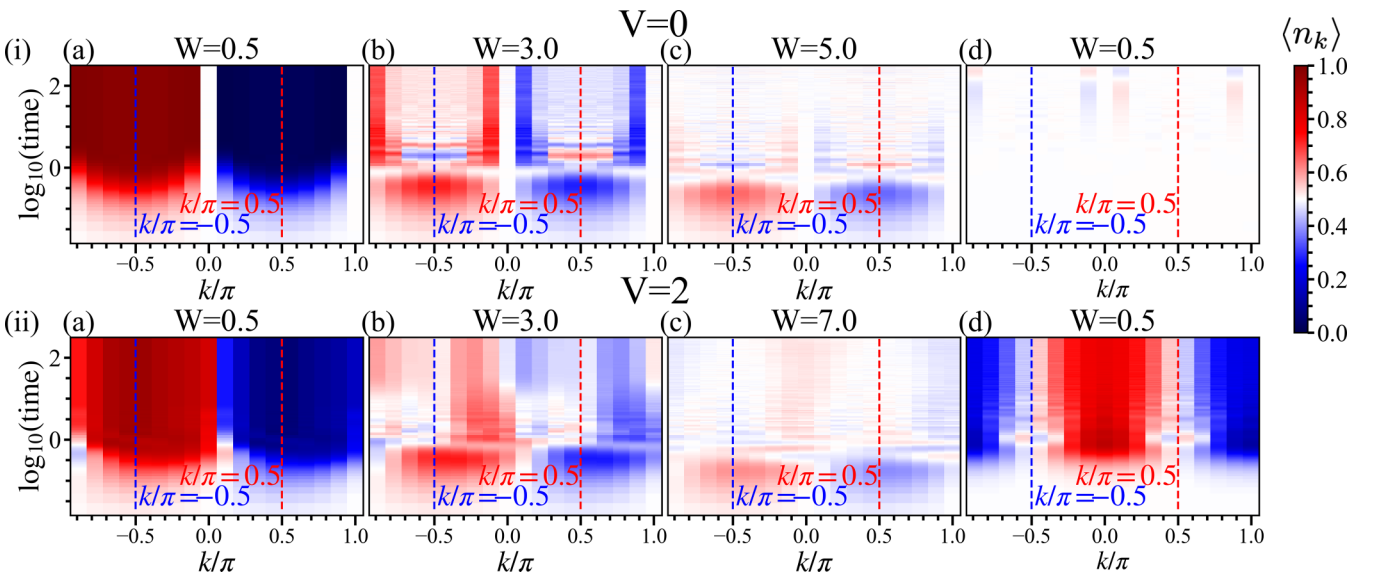


FIG. 3. Evolution of the density profile in the crystal-momentum ( $k$ ) space, i.e.,  $n_k(t)$ . Similarly to Fig. 2, the first row [(i-a)–(i-c)]: noninteracting case ( $V = 0$ ), asymmetric hopping ( $g = 0.5$ ), and (i-d):  $V = 0$ , symmetric hopping ( $g = 0.0$ ). The second row [(ii-a)–(ii-c)]: interacting case ( $V = 2.0$ ),  $g = 0.5$ , and (ii-d):  $V = 2.0$ ,  $g = 0.0$ . We used the same wave functions as in Fig. 2.

of Fig. 3(ii)(a). As  $W$  is increased, e.g., in Fig. 3(b) the distribution is smeared out, and a sharp signature as in Eq. (27) becomes no longer visible. Note that in the crystal-momentum space, both onsite potential  $W_j$  and the interparticle interaction  $V$  are sources of scattering.  $V$  corresponds to two-particle scattering process: two particles with wave number  $k$  and  $k'$  exchange their momenta. These are all very different from the Hermitian case [column 3(d)] where  $n_k(t)$  remains uniform during the time evolution in the noninteracting case [panel (i-d)], while in the second row [panel (ii-d)],  $n_k(t)$  evolves into an equilibrium distribution, which is reminiscent of the one realized in the thermodynamic limit [cf. eigenstate thermalization hypothesis (ETH)]. Interparticle scatterings induced by a finite  $V$  introduces (an effective form of) dissipation in the system (i.e., in the eigenstate), bringing it to an effective thermal equilibrium.

### B. Entanglement dynamics

Figure 4 shows examples of entanglement dynamics at various strength of disorder and in systems of different size. The asymmetry in hopping is fixed at  $g = 0.5$ . Figure 4(a) represents the noninteracting case ( $V = 0$ ), while in Fig. 4(b) a moderate strength of interparticle interaction ( $V = 2.0$ ) is assumed. In the insets of the two panels different curves represent time evolution of the entanglement entropy  $S_{\text{ent}}$  at different strengths of disorder  $W$  but for a system of size fixed at  $L = 18$ .

In the noninteracting case [Fig. 4(a)], the critical strength of disorder  $W_c$  for the localization transition is  $W_c = 2e^g \simeq 3.297\dots$ , so that (i)  $W = 0.5, 1.0, 2.0$  correspond to the regime of weak disorder and delocalized wave function, (ii)  $W = 3$  roughly corresponds to the critical disorder strength  $W_c$ , therefore, may be classified into the critical regime, while (iii)  $W = 4.0, 5.0$  fall on regime of strong disorder and localized wave functions.

In the interacting case, the corresponding values of  $W$  in each regime depend on the strength of the interaction  $V$  since, in principle,  $W_c$  depends on  $V$ . In case of Fig. 4(b), i.e., at  $V = 2.0$ , the classification may be such that regime (i)  $W = 0.5, 1.0, 2.0$ , regime (ii)  $W = 3.0, 4.0, 5.0, 6.0$ , regime (iii)  $W = 7.0, 8.0$ . In the main panel, the size dependence of the entanglement entropy is shown in each of the three different regimes.

In the noninteracting case, in Fig. 4(a), the main panel, after the initial growth  $t > 10^0 - 10^1$ ,  $S_{\text{ent}}(t)$  tends to become saturated: in regime (i) to a value  $\simeq 1.5$ , while in regime (ii) this value is much enhanced, and in regime (iii) the saturated value gets back to the ones comparable to those in regime (i). Thus, as the strength  $W$  of disorder is varied (increased), the saturated value of the entanglement entropy changes nonmonotonically; it is first enhanced by  $W$ , then suppressed.

In the interacting case [Fig. 4(b)], the behavior of  $S_{\text{ent}}$  in regime (i) is similar to the noninteracting case, while the behavior of  $S_{\text{ent}}$  changes qualitatively in regimes (ii) and (iii). In regime (ii),  $S_{\text{ent}}(t)$  is much enhanced in the intermediate time range  $t \sim 10^0 - 10^1$ , but tends to be suppressed afterwards  $t > 10^2$ ;  $S_{\text{ent}}(t)$  shows a nonmonotonic growth in this regime. In regime (iii)  $S_{\text{ent}}(t)$  continues to grow after the initial growth, i.e.,  $S_{\text{ent}}(t) \sim \log t$  at  $t \gg 10^0$ , behavior characteristic to the

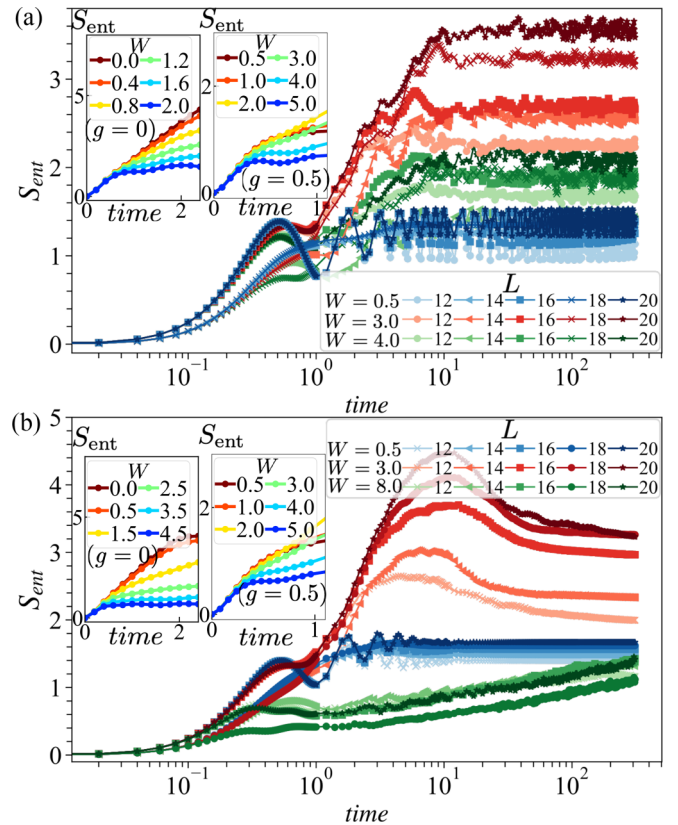


FIG. 4. Entanglement dynamics in three different regimes of disorder strength: delocalized, critical, and localized regimes. Size dependence of the entanglement entropy is also shown. (a) Noninteracting case:  $V = 0$ , (b) interacting case:  $V = 2$ . In numerical calculation, we carried out evaluations for different system sizes using varying sample sizes for  $V = 2$ . We employed 100, 100, 100, 80, and 40 samples for  $L = 12, 14, 16, 18$ , and  $20$ , respectively. Similarly, for  $V = 0$ , we used 100, 40, 40, 40, and 20 samples for  $L = 12, 14, 16, 18$ , and  $20$ . We choose the length of subsystem  $\ell$  to be  $\ell = L/2$ . In inset panels of (a), we conducted evaluations for  $L = 18$  with 80 samples (for Hermitian case) and 40 samples (for non-Hermitian case). In inset panels of (b), we conducted evaluations for  $L = 18$  with 80 samples (for both Hermitian and non-Hermitian cases).

many-body localized regime [77–81]. Thus, as the strength  $W$  of disorder is varied (increased), the overall magnitude of  $S_{\text{ent}}(t)$  in its dynamics is again nonmonotonic as in the noninteracting case. This is quite a curious behavior if we recall that in the Hermitian case many-body states become less entangled with the increase of  $W$  [82,83]. Here, the many-body states tend to become more entangled with the increase of  $W$ , i.e., in the weakly disordered regime (i), while they tend to become less entangled beyond a certain critical value  $W > W_c$  [in regime (iii)]. Such nonmonotonic dependence on  $W$  is a characteristic non-Hermitian feature. In the critical regime [regime (ii)], on the other hand, another nonmonotonic feature is emergent in the entanglement dynamics, i.e., the nonmonotonic time evolution of the entanglement entropy  $S_{\text{ent}}(t)$  in time.

A careful reader may notice on top of the above overall feature that  $S_{\text{ent}}$  exhibits also a rapid oscillation typically in

the weakly disorder regime. The oscillation tends to damp in the course of time in the interacting case [Fig. 4(b)], while it remains in the noninteracting case [Fig. 4(a)]. The oscillation is also conspicuous in the case of even number of particles  $L/2 = 6, 8, 10$ , while less pronounced in the case of odd number of particles  $L/2 = 7, 9$ . We show, in Appendix D, that the oscillation stems from a twofold degeneracy (in the imaginary part) of the asymptotic state.

#### IV. QUASIPARTICLE PICTURE

The entanglement dynamics in a Hermitian system and in (or close to) the clean limit ( $W = 0$ ) is well described by the quasiparticle picture. Here, we discuss, how the entanglement dynamics in a non-Hermitian system we have sketched in the previous section can or cannot be compatible with this picture.

The observed behavior of the density dynamics in the crystal-momentum space introduced earlier (see Sec. III) is directly relevant to the description of the quasiparticle picture. In Fig. 3 and related descriptions, we have seen that  $\langle n_k \rangle$  is almost uniform ( $\langle n_k \rangle \simeq \frac{1}{2}$ ) in the Hermitian case, while  $\langle n_k \rangle$  converges to  $\langle n_k \rangle = 1$  for  $k < 0$ , and  $\langle n_k \rangle = 0$  for  $k > 0$  in the non-Hermitian case. The two panels of Fig. 1 are in a sense a pictorial representation of these contrasting behaviors, i.e., Fig. 1(a) corresponds to Fig. 3(i-d) (the Hermitian case) and Fig. 1(b) corresponds to Fig. 3(i-a) [the non-Hermitian case (close to the clean limit)].

##### A. GGE vs nonunitary dynamics

Let us focus on the clean and noninteracting limits ( $W = 0$  and  $V = 0$ ). First, in the Hermitian case, in this case,  $\hat{n}_k = c_k^\dagger c_k$  is a conserved quantity [ $\hat{n}_k, H$ ] = 0. In this integrable system, the expectation value, such as  $\langle \hat{n}_k \rangle = \langle \Psi | \hat{n}_k | \Psi \rangle$ , is also expressed as a statistical average in the so-called generalized Gibbs ensemble (GGE) characterized by an infinite number of Lagrange multipliers  $\lambda_k$ , each associated with the conservation of  $n_k$  (see Appendix E for details). To be explicit,  $n_k$  can be expressed as

$$\langle \hat{n}_k \rangle = \frac{1}{1 + e^{\lambda_k}}, \quad (28)$$

where for the density-wave-like initial state (4) all  $\lambda_k$  are equal to 0 [84], i.e.,  $\langle \hat{n}_k \rangle = \frac{1}{2}$ . We have seen this in the density dynamics studied in Sec. III. In Fig. 3, in all the panels, the initial and early time density distribution  $n_k(t = 0)$  shows such a uniform profile ( $\langle \hat{n}_k \rangle \simeq \frac{1}{2}$ ), while in the first row, panel (i-d), i.e., in the noninteracting ( $V = 0$ ) and Hermitian ( $g = 0$ ) case, such an initial profile is maintained, though approximately, due to a small but finite  $W = 0.5$ . Note that the (entanglement) entropy associated with a generalized Gibbs ensemble specified by the distribution (28) is given as (see Appendix E for its derivation)

$$s(k) = -\langle \hat{n}_k \rangle \log(\langle \hat{n}_k \rangle) - (1 - \langle \hat{n}_k \rangle) \log(1 - \langle \hat{n}_k \rangle). \quad (29)$$

Note that this takes a maximal value  $\log 2$  at  $\langle \hat{n}_k \rangle = \frac{1}{2}$  ( $\lambda_k = 0$ ).

In the *non-Hermitian* case with  $\text{Im}(\epsilon_k) \neq 0$  ( $\epsilon_k$  is a single-particle eigenenergy), if we repeat the same argument leading

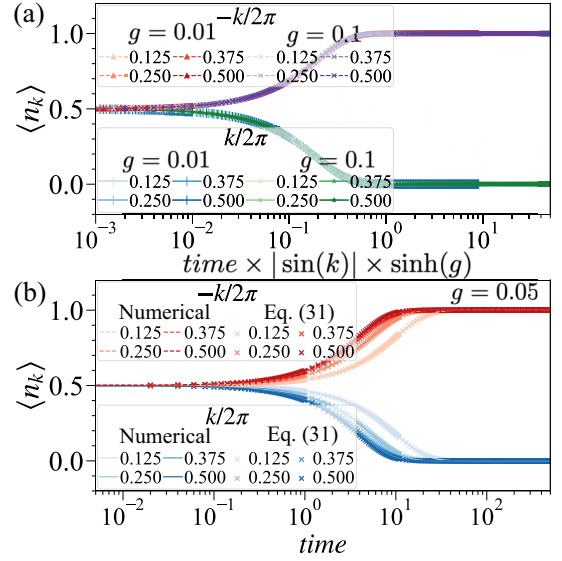


FIG. 5. Time-dependence of  $\langle \hat{n}_k \rangle$ : (a)  $\langle n_k \rangle$  versus  $time \times |\sin(k)| \times \sinh(g)$  with the various values of  $g$ , (b)  $\langle n_k \rangle$  (scatter plot) and Eq. (31) (solid or dashed line) versus  $time$ . For panel (b),  $g$  is fixed at  $g = 0.05$ . Numerical calculation is conducted by the following parameter:  $L = 16$ ,  $W = 0$ , and  $V = 0$ .

to Eq. (28), one is left with (see Appendix E)

$$\langle \hat{n}_k \rangle = \frac{1}{1 + e^{\lambda_k - 2\text{Im}(\epsilon_k)t}}, \quad (30)$$

i.e.,  $\langle \hat{n}_k \rangle$  is no longer conserved in this case. Again, for the initial DW-like pattern (4), all  $\lambda_k$ 's are to be set to 0 in Eq. (30). Noticing that  $\text{Im}(\epsilon_k) > 0$  for  $k < 0$ ,  $\text{Im}(\epsilon_k) < 0$  for  $k > 0$ , and thus  $\langle \hat{n}_k \rangle$  converges either to 0 ( $k > 0$ ) or to 1 ( $k < 0$ ). In Fig. 5, we have plotted the calculated value of  $n_k(t)$  against the scaling function

$$\langle \hat{n}_k \rangle = \frac{1}{1 + e^{-2\text{Im}(\tilde{\epsilon}_k)t}}, \quad (31)$$

where  $\tilde{\epsilon}_k = 2\epsilon_k$ . Figure 5 shows that the numerical data fit quite well with the scaling function (31) expected in GGE except for a factor 2 in the definition of  $\tilde{\epsilon}_k$ .<sup>5</sup>

As shown also in a more generic context in Appendix E [see, e.g., Eqs. (E4) and (E5)], the time dependence of  $\langle \hat{n}_k \rangle$  [here, e.g., Eq. (30)] is analogous to that of the imaginary-time evolution driven by a *Hermitian* Hamiltonian, often employed in a numerical recipe to find the ground state, e.g., in a path-integral quantum Monte Carlo, or in a tensor-network method [85]. In the imaginary-time evolution, the parameter  $t$  (time) corresponds to a “temperature” of the statistical ensemble. Thus, an evolution driven by a non-Hermitian matrix leads

<sup>5</sup>That is,  $\langle \hat{n}_k \rangle$  suggested by GGE (see Appendix E for more details) converges either to 0 or to 1 more slowly than Eq. (31). This discrepancy is because we assume superposition consists of various filling to derive Eq. (E6), whereas in the actual numerical calculation, we consider the half-filling case. If the initial state is prepared as a superposition consists various filling  $Q = \sum_i k_i/L$ , the time dependence of  $\langle \hat{n}_k \rangle$  is akin to Eq. (E6) (see Appendix F).

to an effective decrease in temperature. Consequently, as time passes by, the temperature decreases, and the entropy ( $S_{\text{ent}}$ ) also seems to decrease. In the following subsection, we investigate how  $S_{\text{ent}}$  behaves under a nonunitary dynamics.

### B. Entanglement dynamics in the quasiparticle picture in the clean and noninteracting limits ( $W = 0$ and $V = 0$ )

In the quasiparticle picture, the initial state  $|\Psi(t=0)\rangle$  consists of a superposition of a highly excited state, acting as a source of quasiparticle excitations. Pairs of quasiparticles with opposite momenta  $k$  and  $-k$  are emitted at the same point, and as times passes by, they move, in the Hermitian case, symmetrically in opposite directions. This is schematically depicted in Fig. 1(a). Once each quasiparticle is located in the different subsystem,  $S_{\text{ent}}$  increases. This process is formulated by

$$S_{\text{ent}}(t) \propto 2t \int_{2v(k)t < \ell} dk v(k) s(k) + \ell \int_{2v(k)t > \ell} dk s(k), \quad (32)$$

where  $\ell$  is the subsystem size,  $k$  is a momentum of quasiparticles,  $v(k)$  is its velocity, and  $s(k)$  determines the production rate of  $S_{\text{ent}}$ . This production rate tightly relates to the entropy of statistical mechanics because  $s(k) = -\langle \hat{n}_k \rangle \log(\langle \hat{n}_k \rangle) - (1 - \langle \hat{n}_k \rangle) \log(1 - \langle \hat{n}_k \rangle)$ .

Entanglement dynamics (32) has a characteristic timescale  $t_c(k)$  determined by  $\ell$  and  $v(k)$ . When  $t_c(k) \equiv \frac{\ell}{2v(k)} > t$ , each of the quasiparticles emitted at the same points begin to be located in the different subsystems, contributing to the entanglement production as a function of  $s(k)v(k)t$ . While  $t_c(k) < t$ , most of each of the quasiparticles are located in the different subsystems; therefore, the contribution of  $S_{\text{ent}}$  from pairs of quasiparticles  $s(k)$  becomes constant value  $s(k)\ell$ .<sup>6</sup>

In the non-Hermitian case, as time passes by, one of the quasiparticles is amplified while the other is attenuated due to  $\text{Im}(E)$ , resulting in a unidirectional motion [depicted in Fig. 1(b)]. Moreover, this characteristic relaxation of  $\langle \hat{n}_k \rangle$  (31) results in a variation of  $\langle \hat{n}_k \rangle$  from  $\langle \hat{n}_k \rangle = 0.5$ , indicating a decrease in  $S_{\text{ent}}$  as suggested by Eqs. (31) and (32). Therefore, we investigate how the non-Hermiticity, specifically this characteristic relaxation, modifies the quasiparticle picture and entanglement dynamics. Figures 6(a) and 6(b) show  $S_{\text{ent}}$  as a function of  $time$  and  $time \times \cosh(g)$ , respectively, with various values of  $g$ , in the clean and noninteracting limits ( $W = 0$  and  $V = 0$ ). We observe distinct behaviors of  $S_{\text{ent}}(t)$  arising from the quasiparticle picture and nonunitary time evolution. We first focus on the initial growth of  $S_{\text{ent}}$ . According to the quasiparticle picture, the initial growth of  $S_{\text{ent}}$  depends on  $v_g t$  ( $v_g$  is a group velocity), and see Eq. (32) rather than  $e^g t$  since  $S_{\text{ent}}$  is carried by quasiparticles as well as correlation. In this case,  $v_g = -2 \cosh(g) \sin(k)$ , and thus we expect that the initial growth of  $S_{\text{ent}}$  depends on  $\cosh(g) \sin(k)t$ . We observe that the initial growth of  $S_{\text{ent}}$  can be approximated by

<sup>6</sup>Strictly speaking, since we treat a finite system, each quasiparticle can be located in the same subsystem due to the boundary effect (we later comment on this effect), leading to decay in the  $S_{\text{ent}}$ . Although this effect can be non-negligible in a finite system, it is already known that the less important this effect, the larger the system size we treat [86]; therefore, we can interpret  $t_c(k)$  as a characteristic timescale.

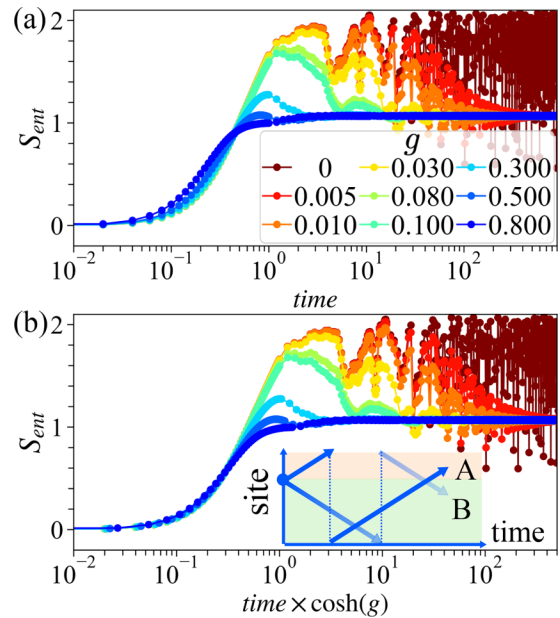


FIG. 6. Entanglement dynamics of a free-particle case ( $W = 0.0$  and  $V = 0.0$ ) with  $\ell = 3$  with decrease of  $g$ : (a)  $S_{\text{ent}}$  versus  $time$  and (b)  $S_{\text{ent}}$  versus  $time \times \cosh(g)$  (analogy of quasiparticle picture).  $L = 16$ .

a single curve, as is shown in Fig. 6(b), consistent with the quasiparticle picture and implying the validity of the quasiparticle picture at early timescales. Following the initial growth,  $S_{\text{ent}}(t)$  depends on  $g$ .  $S_{\text{ent}}(t)$  shows nonmonotonic behavior for weak  $g$ , whereas it only converges to  $S_{\text{ent}}(|\alpha_1|)$  for strong  $g$ . This difference in  $S_{\text{ent}}(t)$  between weak and strong  $g$  stems from the relaxation of  $\langle \hat{n}_k \rangle$ . For weak  $g$ , Eq. (31) implies that the relaxation of  $\langle \hat{n}_k \rangle$  takes a considerable amount of time, causing  $S_{\text{ent}}(t)$  to resemble the behavior observed in the Hermitian case within this regime, leading to  $S_{\text{ent}}(t) > S_{\text{ent}}(t \rightarrow \infty)$ . However,  $\text{Im}(E)$  eventually causes  $\langle \hat{n}_k \rangle$  to converge to either 0 or 1, thereby resulting in the convergence of  $S_{\text{ent}}(t)$  to  $S_{\text{ent}}(\infty)$  and nonmonotonic behavior of  $S_{\text{ent}}$ .<sup>7</sup> Additionally, we also observe Hermitian-type behavior in which the nonmonotonic behavior of  $S_{\text{ent}}$  is accompanied by oscillations. These oscillations occur when quasiparticles move through the left or right ends [see inset of Fig. 6(b)] and are located within the same subsystem. This oscillation behavior is known for entanglement revivals [86], predicted by the quasiparticle picture. For large  $g$ ,  $\langle \hat{n}_k \rangle$  immediately converges to either 0 or 1, and thus  $S_{\text{ent}}(t)$  only converges to  $S_{\text{ent}}(\infty)$ .

As we have observed, the interplay between the quasiparticle picture and the relaxation described by Eq. (31) qualitatively captures entanglement dynamics of the HN model. In Appendix (G), we compare the numerical result with  $S_{\text{ent}}$  suggested by the quasiparticle picture to verify

<sup>7</sup>In numerical calculation, we choose the length of subsystem size  $\ell$  to be small because it may be the simplest way to realize the nonmonotonic behavior of  $S_{\text{ent}}$ . Since  $S_{\text{ent}}(t \rightarrow \infty)$  decreases with a decrease of  $\ell$ , in case of small  $\ell$ , the condition  $S_{\text{ent}}(t) > S_{\text{ent}}(t \rightarrow \infty)$ , which is required to realize such a behavior, becomes easier to achieve.



the accuracy of this picture. While this picture provides a qualitative characterization of  $S_{\text{ent}}(t)$ , we find a quantitative discrepancy between the numerical result and  $S_{\text{ent}}$  suggested by this picture. Further work is required to identify the reason why this quantitative discrepancy presents.

### C. Disordered case: Disorder enhances the entanglement

The quasiparticle picture also provides us with a natural interpretation on why disorder enhances the entanglement in the non-Hermitian case. First, in the Hermitian case, as disorder is introduced to the system, here in our analysis, in the form of a quasiperiodic potential, the entanglement entropy tends to be suppressed (see, e.g., inset of Fig. 4). This is because such a quasiperiodic potential introduces scattering between quasiparticles, preventing quasiparticle pairs from reaching a different subsystem [Fig. 1(a)]. If the pairs tend to stay in the same subsystem, the entanglement entropy tends naturally to be decreased. In the non-Hermitian case, scattering between quasiparticles introduced by the quasiperiodic potential may lead to quite a different consequence. As repeatedly mentioned, the quasiparticle motion is unidirectional in the absence of scattering [Fig. 1(b)], while in the presence of scattering this is expected to be no longer purely unidirectional, but become more bidirectional. As a result, disorder helps quasiparticle pairs to reach a different subsystem, leading naturally to the increase of entanglement entropy.

In the density dynamics (Fig. 3), we have seen that  $\langle n_k \rangle$  converges sharply to 0 or 1 in the clean limit, while in the presence of disorder, this convergence is relaxed. This clearly leads to the increase of thermodynamic entanglement entropy [Eq. (29)] (see Appendix E for more details). In the interacting case, the behavior of  $\langle n_k \rangle$  is not much different from the noninteracting case [Fig. 3(ii)], the above reasoning in the noninteracting case applies also, at least qualitatively, to the interacting case.

Previously, we have attributed this enhancement of the entanglement entropy due to disorder to cascadelike spreading of the wave packet in the single-particle dynamics [44,87]. Here, we have shown that the quasiparticle picture gives a more natural explanation of the same phenomenon, which is more likely valid in the interacting case.

### V. LOGARITHMIC SCALING IN THE ASYMPTOTIC REGIME: $t \rightarrow \infty$

In the previous subsection, we have seen characteristic behaviors of the entanglement entropy  $S_{\text{ent}}(t)$ , which reflects the collapse of the superposition in the time-evolving many-body state  $|\Psi(t)\rangle$ , i.e., its convergence to a single eigenstate (16). In the Hermitian system, the asymptotic value of the entanglement entropy,

$$S_{\infty} = S_{\text{ent}}(t \rightarrow \infty), \quad (33)$$

obeys the volume-law scaling. Here, we address what type scaling  $S_{\infty}$  shows in the non-Hermitian case. For a given entire system of size  $L$  (here, we fix it at  $L = 20$ ), we vary the bipartite division  $\ell$ , i.e., the size of the subsystem A, and evaluate the entanglement entropy  $S_{\infty}(\ell)$  in the asymptotic regime  $t \rightarrow \infty$ . Figure 7(a) shows a result of such analyses in

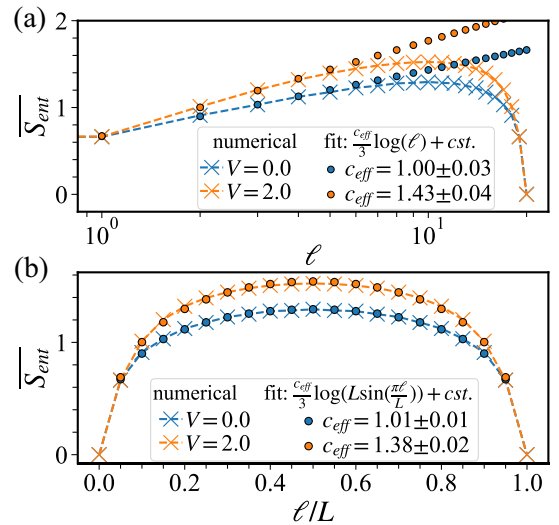


FIG. 7. Scaling of  $S_{\text{ent}}$  as a function of  $\ell$ , where  $\ell$  is a length of subsystem: (a)  $S_{\text{ent}}$  versus  $\ell$ , (b)  $S_{\text{ent}}$  versus  $\ell/L$ . For (b), we take into account the boundary condition, so that fitting function  $\frac{c_{\text{eff}}}{3} \log[L \sin(\frac{\pi \ell}{L})] + \text{cst.}$  (Scatter plot) Seems to be fitted to the numerical data (dashed line). cst is corresponding to a constant value.  $g = 0.5$ .  $W = 0.0$ .

the case of  $W = 0$ ,  $V = 0$ , in which  $S_{\infty}(\ell)$  is plotted against  $\log \ell$ . One can see that for  $\ell \ll L$  at which size effects are negligible, the entanglement entropy  $S_{\infty}(\ell)$  is well fit by the scaling function

$$S_{\infty}(\ell) = \frac{1}{3} \log \ell + \text{cst}, \quad (34)$$

known in the Hermitian case for a fermionic ground state, which falls on the case of central charge  $c = 1$  (case of free bosonic excitation spectrum) [88–93].

One can even improve the fitting by taking into account the finite size of the system and the periodic boundary condition; replacing the length  $\ell$  of the subsystem A in Eq. (34) with the corresponding chord distance

$$d(\ell) = 2L \sin(\pi \ell / L) \quad (35)$$

of a circle of circumference  $L$ , one finds

$$S_{\infty}(\ell) = \frac{1}{3} \log [2L \sin(\pi \ell / L)] + \text{cst}. \quad (36)$$

In Fig. 7(b) the same data of the entanglement entropy  $S_{\text{ent}}$  are plotted against the subsystem size  $\ell$  in linear scale and fit by the scaling function (36). One can see all the data  $\ell = 1, 2, \dots, L - 1$  of  $S_{\text{ent}}$  are well fit by this modified scaling function.

In case of the fermionic ground state,

$$|\Psi_G\rangle = \left( \prod_{k \text{ s.t. } |k| < k_F} c_k^\dagger \right) |0\rangle, \quad (37)$$

the logarithmic term in Eq. (34) stems from discontinuities in the momentum space at  $k = k_F$  and  $-k_F$ , where  $k_F$  is the Fermi wave number or Fermi (crystal) momentum associated with the Fermi energy  $\epsilon_F = \hbar^2 k_F^2 / (2m)$ . In the asymptotic expansion for large  $L$ , the subleading logarithmic term becomes relevant as a result of the vanishing of the leading linear

term  $\propto L$  (volume-law term). In the non-Hermitian dynamics the many-body wave packet  $|\Psi(t)\rangle$  may converge to a single eigenstate (26). Then, the corresponding momentum distribution (27) exhibits discontinuities at  $k = 0$  and  $-\pi$  in case of the half-filling. These discontinuities lead to logarithmic scaling of the entanglement entropy (34), known in the fermionic ground state [94,95].

In the interacting case, the entanglement entropy  $S_\infty(\ell)$  seems still logarithmic [Fig. 7(b)], in the sense that the data are well fit by the following scaling function:

$$S_\infty(\ell) = \frac{c_{\text{eff}}}{3} \log [2L \sin(\pi \ell/L)] + \text{cst}, \quad (38)$$

where  $c_{\text{eff}}$  is a fitting parameter; of course, the naming implies that we are tempted to interpret it as an effective central charge. Our data clearly show that  $c_{\text{eff}}$  exhibits a deviation from the noninteracting value  $c = 1$ , which is uncommon in the Hermitian case [96]. Another remark is that in the regime of larger  $V$  we found a discrepancy of our data with the fitting function (38); see Appendix H for more details. The discrepancy may be simply due to a finite-size effect, but in any case a further investigation in a system of larger size  $L$  will be necessary, employing the methods such as Bethe ansatz [97–99], the tensor network [99–103], and the quantum Monte Carlo simulation [104–107].

## VI. FURTHER SCALING PROPERTIES: BEHAVIOR OF $\text{Im}(E)$ AND CORRELATION FUNCTION

### A. Imaginary part of the eigenenergy: Origin of the nonmonotonic time evolution

In Sec. III, we have seen that the entanglement entropy  $S_{\text{ent}}(t)$  exhibits a nonmonotonic time evolution, typically, in the regime of intermediate disorder and in the interacting case [Fig. 4(b)]. A sensible reader would immediately associate this intriguing behavior, unique also to the non-Hermitian case, with the complex nature of the spectrum characteristic to the system, which is indeed the case. While, if that is simply the reason, one may then wonder why the nonmonotonic evolution is specific to the interacting case, and does not appear in the noninteracting case [Fig. 4(a)], albeit that the complex spectrum also appears in noninteracting case. Below, we will carefully focus on the complex nature of the spectrum, highlighting especially the degeneracy in the imaginary part of the spectrum  $\text{Im}(E)$ . The crucial difference that also leads to the conspicuous difference in the behavior of entanglement entropy  $S_{\text{ent}}(t)$  in the interacting vs noninteracting cases lies in the difference (absence vs presence) of such degeneracy in  $\text{Im}(E)$  in the complex spectrum. After briefly looking into the scaling of the  $\text{Im}$  ratio  $f_{\text{Im}}$ , relevant to the identification of the real-complex transition in spectrum, we will proceed to a more careful study of such degeneracies in  $\text{Im}(E)$ .

The fraction  $f_{\text{Im}}$ , which is defined as the ratio of the number of the eigenenergies with nonzero imaginary part ( $|\text{Im}(E)| > 10^{-10}$ )  $D_{\text{Im}}$  to the total number of the eigenenergies  $D$ , i.e.,

$$f_{\text{Im}} = D_{\text{Im}}/D, \quad (39)$$

is often employed in the study of real-complex transition [63,65,75].  $f_{\text{Im}}$  is typically averaged within a defined energy

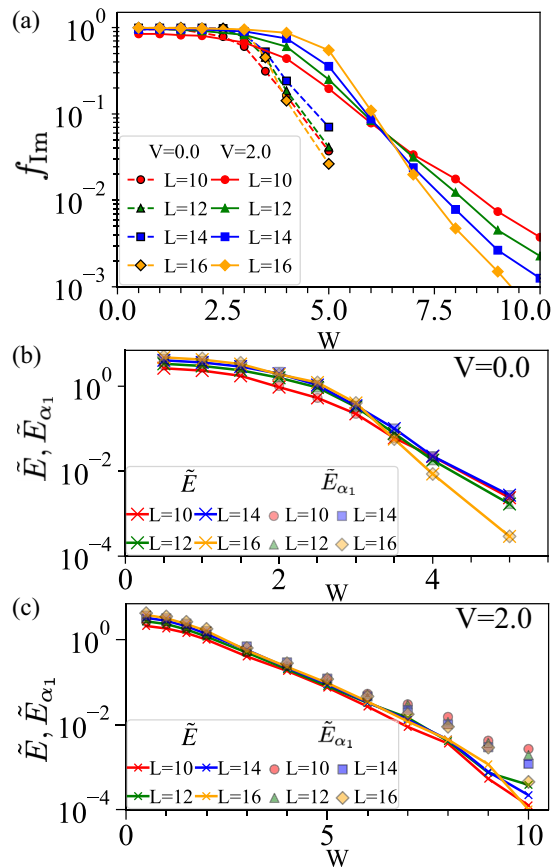


FIG. 8. Disorder dependence of the quantity to characterize the property of  $\text{Im}(E)$  for various system sizes  $L$ . (a)  $f_{\text{Im}}$  for noninteracting ( $V = 0$ , dashed line) and interacting ( $V = 2$ , solid line) cases, respectively. The largest  $\text{Im}(E)$ ,  $\tilde{E}_{\alpha_1} \equiv \text{Max}[\text{Im}(E)]$  (scatter plot), and the average value of  $\text{Im}(E)$  taken from the second to fifth,  $\tilde{E}$  (solid line) for noninteracting (b) and interacting (c) cases, respectively. In numerical calculation, we carried out evaluations for various system sizes  $L = 10, 12, 14$ , and  $16$  using varying sample sizes: 1000, 500, 500, and 200 samples for  $L = 10, 12, 14$ , and  $16$ .

range or across the entire spectrum. Thus, we can consider  $f_{\text{Im}}$  as a measure to describe the statistical properties of a complex spectrum. In the delocalized phase,  $f_{\text{Im}}$  is close or almost equal to 1, whereas it practically vanishes in the localized phase.  $f_{\text{Im}}$  in the noninteracting case shown in Fig. 8(a) (dashed line) takes almost constant value  $f_{\text{Im}} \sim 1$  for weak  $W$ , and as  $W$  approaches  $W_c \sim 3.3$ ,  $f_{\text{Im}}$  sharply decreases. This tendency becomes more enhanced as  $L$  increases, and in the  $(W, f_{\text{Im}})$  plane, different curves for  $f_{\text{Im}}$  calculated at different system size  $L$  looks intersecting at a single point  $(W_c, f_{\text{Im}}(W_c))$  [Fig. 8(a)], implying that this real-complex transition at  $W = W_c$  is a true phase transition robust until the thermodynamic limit  $L \rightarrow \infty$ . In the interacting case (solid line), the position of the crossing is shifted to a regime of larger  $W$  compared with the noninteracting case (dashed line), while the overall behavior is unchanged from the noninteracting case. Thus, so far as the scaling analysis of  $f_{\text{Im}}$  implies, the real-complex transition of the spectrum occurs practically in the same way both in the interacting and noninteracting cases. Then, how could that be compatible with a relatively different dynamics

of the entanglement entropy  $S_{\text{ent}}(t)$  in the interacting and noninteracting cases?

In Sec. II A, we have argued that in the nonunitary time evolution the many-body wave packet  $|\Psi(t)\rangle$ , which is initially a superposition of many eigenstates, tends to lose such a superposed nature, and collapses into a single eigenstate  $|\alpha_1\rangle$  [see Eq. (16)], where  $|\alpha_1\rangle$  is such an eigenstate whose eigenenergy  $E$  has a maximal imaginary part  $\text{Im}(E)$ . This picture demonstrated in Sec. II A is, however, slightly oversimplified in the sense that it did not consider the case in which some eigenstate has (practically) the same, or very close  $\text{Im}(E)$ , the case in which

$$\text{Im}(E_{\alpha_1}) \simeq \text{Im}(E_{\alpha_2}) \simeq \dots \quad (40)$$

Which quantity is relevant for determining how quickly the state  $|\Psi(t)\rangle$  converges (or not) to a single eigenstate  $|\alpha_1\rangle$ ?  $\text{Im}(E_{\alpha_v}) > 0$  amplifies the amplitude of the coefficient  $c_{\alpha_v}(t)$ , expressed as  $|c_{\alpha_v}(t)|^2 = |c_{\alpha_v}(t=0)|^2 e^{\text{Im}(E_{\alpha_v})t}$ . The relative importance of the state  $|\alpha_1\rangle$  with respect to another state, e.g.,  $|\alpha_v\rangle$  in the time-evolving wave packet  $|\Psi(t)\rangle$  may be quantified by the ratio

$$\frac{|c_{\alpha_v}(t)|^2}{|c_{\alpha_1}(t)|^2} \propto |e^{\text{Im}[2(E_{\alpha_v} - E_{\alpha_1})t]}| = e^{-\Delta_{\text{Im}}^v t}. \quad (41)$$

Here, we consider the quantity  $\tilde{E}$  defined as the average of the second to the fifth largest value of  $\text{Im}(E)$ , and conjecture that the difference between  $\tilde{E}_{\alpha_1} \equiv \text{Max}[\text{Im}(E)]$  would be a good measure for characterizing how quickly the state  $|\Psi(t)\rangle$  converges to (or not to) a hypothetical asymptotic state  $|\alpha_1\rangle$ .

Figures 8(b) and 8(c) show  $\tilde{E}_{\alpha_1}$  and  $\tilde{E}$  as a function of  $W$  in the noninteracting and interacting case, respectively. Both  $\tilde{E}_{\alpha_1}$  and  $\tilde{E}$  decrease with an increase of  $W$ , leading to a decrease in  $\Delta_{\text{Im}}^v$  [cf. Eq. (41)]. Interestingly, in the localized phase of the noninteracting system,  $\tilde{E}$  is the same as  $\tilde{E}_{\alpha_1}$ , which means  $\tilde{E}_{\alpha_1}$  is degenerate. When  $\tilde{E}_{\alpha_1}$  is degenerate, the corresponding eigenstates are amplified under time evolution similarly, i.e.,  $\Delta_{\text{Im}}^v = 0$ , and thus superposition  $c_{\alpha_v}(t)$  is maintained [cf. Eq. (41)] even in the nonunitary time evolution. Such a degeneracy stems from the fact that  $\text{Im}(E_{\alpha_v})$  is a sum of single-particle eigenenergies  $\epsilon_\alpha$ 's. In the localized phase, most of  $\epsilon_\alpha$  are real spectra, but some  $\epsilon_\alpha$  have nonzero imaginary parts of eigenenergies due to the finite-system-size effect, causing the combination of the sum of the real and complex spectra to lead to the degeneracy of  $\text{Im}(E)$ . In contrast to the noninteracting case, in an interacting case,  $\tilde{E}_{\alpha_1}$  is not the same as the  $\tilde{E}$ , which means that  $|\Psi(t)\rangle$  generally converges to a single eigenstate  $|\alpha_1\rangle$  and nonmonotonic behavior of  $S_{\text{ent}}$  appears consequently.

## B. Entanglement entropy and correlation function

Finally, we focus on how the scaling of the entanglement entropy  $S_{\text{ent}}$  and the correlation function as a function of the strength  $W$  of disorder. In Fig. 9(a),  $S_\infty = S_{\text{ent}}(t \rightarrow \infty)$  [same as in Eq. (33)], evaluated in a system of size  $L$ ; so we will also call  $S_\infty(L)$ , ensemble averaged, plotted as function of  $L$ , i.e., how  $S_\infty(L)$  scales with  $L$  at a various strength of disorder  $W$  in the noninteracting limit ( $V = 0$ ). One remarkable point is that the plotted curves  $S_\infty(L)$  show a nonmonotonic evolution as a function of  $W$ . For weak  $W$ ,  $S_\infty(L)$  obeys the

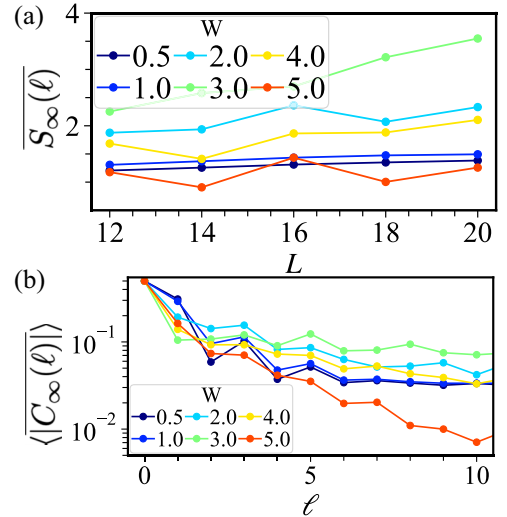


FIG. 9. Size dependence of the entanglement entropy  $S_\infty(L)$  (the asymptotic value) (a) and behavior of the correlation function  $C_\infty(\ell)$  (b) both in the noninteracting limit. (a)  $S_\infty = S_{\text{ent}}(t \rightarrow \infty)$  is calculated in the system of size  $L$  and plotted as function of  $L$ . Partly, the same data as the ones in Fig. 4 have been replotted. (b) Behavior of the correlation function  $C_\infty(\ell) = C_\infty(\ell, t \rightarrow \infty) = \langle c_j^\dagger c_{j+\ell} \rangle$ , site and sample averaged [as for precise definitions and conditions, see Eqs. (43), (45), and main text]. The same wave functions as those in Fig. 4 have been used.

logarithmic scaling, as we saw in the previous section, while as  $W$  approaches the critical value  $W_c$ , a sharp distribution of  $\langle \hat{n}_k \rangle$  in the crystal-momentum space in the manner of Eq. (27) tends to be lost, and simultaneously  $S_\infty(L)$  starts to obey the volume law. In this critical regime,  $\langle \hat{n}_k \rangle$  takes values other than 0 or 1, implying an increase in the thermodynamic entropy [cf. Eq. (32)]. Once  $W$  exceeds  $W_c$ , scaling of  $S_\infty(L)$  turns to the area law, as is also the case in a Hermitian localized phase. The evolution of the scaling behavior of  $S_\infty(L)$  or  $S_\infty(L, W)$  may be summarized as

$$S_\infty(L) \sim \begin{cases} \log L & (W \ll W_c), \\ L & (W \simeq W_c), \\ 1 & (W > W_c). \end{cases} \quad (42)$$

Another interesting issue is that the behavior of the correlation function

$$C_j(l, t) = \langle \psi(t) | c_j^\dagger c_{j+l} | \psi(t) \rangle \quad (43)$$

shows a similar “nonmonotonic” dependence on  $W$  as the one seen in the entanglement entropy (42). Figure 9(b) shows how this correlation function

$$C_\infty(l) = \lim_{t \rightarrow \infty} C(l, t) \quad (44)$$

decays with the distance  $\ell$ , again, in the noninteracting case. To be precise, in the panel the magnitude (absolute value) of the correlation function, both ensemble and site averaged

$$\langle |C_\infty(l)| \rangle = \left\langle \frac{1}{L} \sum_j |C_j(l, t \rightarrow \infty)| \right\rangle \equiv C_\infty(l) \quad (45)$$

has been plotted. The brackets  $\langle \dots \rangle$  represent the ensemble average. At weak  $W$ , it is expected to show an algebraic

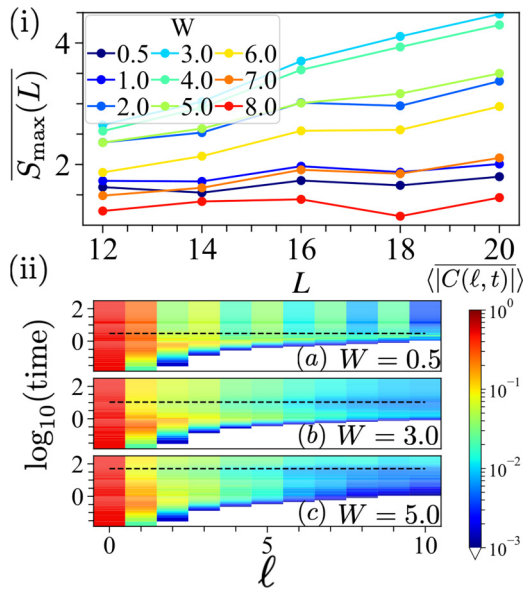


FIG. 10. Scaling of  $S_{\max}(L)$  at various strength of disorder  $W$  (i), and behavior of the correlation function  $C(l, t)$  in the space-time  $(l, t)$  (ii). (i)  $S_{\max}(L)$  [introduced in Eq. (47)] is plotted as a function of  $L$ . Partly, the same data as the ones in Fig. 4 have been used. (ii) The behavior of the correlation function  $C(l, t)$ , introduced in Eq. (43), is shown as a color map for three different values of disorder strength  $W$ : (a)  $W = 0.5$ , (b)  $W = 3.0$ , and (c)  $W = 5.0$  (subpanels). We focused on the magnitude of the correlation function  $|C(l, t)|$ , which has been also site and ensemble averaged [cf. Eq. (45)]. The same wave functions as those in Fig. 4 have been used.

decay [108]:

$$C_{\infty}(l) \propto \frac{1 - e^{i\pi l}}{l} \quad (46)$$

reflecting the sharp distribution of  $\langle \hat{n}_k \rangle$  in the crystal-momentum space (27). As  $W$  increases, the decay of the correlation function  $C_{\infty}(l)$  becomes slower; compare the greenish plots with the bluish ones, implying that the non-locality of the system is increased. This is concomitant with the evolution of the scaling of the entanglement entropy  $S_{\infty}(L)$  from logarithmic to volume law [cf. Eq. (42)]. Once  $W$  exceeds  $W_c$ , the correlation function  $C_{\infty}(l)$  decreases exponentially, reflecting the localized nature of the wave function.

In the interacting case ( $V = 2$ ), we focus on the maximal value of  $S_{\text{ent}}(t)$  in its evolution:

$$S_{\max} = \text{Max}[S_{\text{ent}}(t)] \equiv S_{\text{ent}}(t = t_0), \quad (47)$$

instead of  $S_{\infty} = S_{\text{ent}}(t \rightarrow \infty)$  [Eq. (33)]. This is for a practical reason; the Krylov subspace method employed in this work is very effective for reducing the computational difficulty of dealing with a system of large size, while it does not reduce that of a very long-time dynamics.<sup>8</sup> In Fig. 4, we have already seen an overall behavior of  $S_{\text{ent}}(t)$  at different

values of  $W$ , i.e., both in the delocalized and localized phases, and also at different system sizes  $L$ . Here, we have focused on the size dependence  $S_{\max}(L)$  [panel (i) of Fig. 10] in the interacting case. The scaling behavior of  $S_{\max}(L)$  at various values of  $W$  shows that  $S_{\max}(L)$  increases (decreases) with  $W$  in the delocalized (localized) regime, indicating that  $S_{\max}(L)$  is a good measure of delocalization (localization) transition (crossover) in this interesting case, playing a similar role as  $S_{\infty}(L)$  in the noninteracting case.

We also evaluate the correlation function  $C(l, t)$  introduced in Eq. (43) in the interacting case; here, we focus on its time-dependent behavior since we are interested in how the relaxation of a quantum state  $|\Psi(t)\rangle$  due to  $\text{Im}(E)$  is reflected in the behavior of the correlation function. Three panels of Fig. 10(ii) show the time evolution of the correlation function (43) at disorder strength  $W = 0.5$  [Fig. 10(a)],  $3.0$  [Fig. 10(b)], and  $5.0$  [Fig. 10(c)]. The absolute value of the correlation function  $|C(\ell, t)|$  is plotted as a color map in the space of  $\ell$  (the  $x$  axis) and  $\log_{10}(\text{time})$  (the  $y$  axis). The black dashed line in each panel represents the time  $t_0$  when  $S_{\text{ent}}(t)$  takes the maximal value  $S_{\max} = \text{Max}[S_{\text{ent}}(t_0)]$  [see Eq. (47)]. At weak  $W$  [Fig. 10(a)], the correlation spreads rapidly, i.e.,  $C(l, t)$  quickly (i.e., around  $t = t_0$ ) converges to an asymptotic distribution  $C_{\infty}(l)$  [see Eq. (44)] which is spatially modulating, reminiscent of the algebraic decay (46) in the noninteracting case [see also Fig. 9(b), e.g., case of  $W = 0.5$  (blue plots)]. As  $W$  is increased, the spreading of correlation becomes delayed;  $t_0$  becomes larger, while the asymptotic distribution  $C_{\infty}(l)$  becomes a monotonically decreasing function [Figs. 10(b) and 10(c)].

Unlike in the noninteracting case, we have not observed a nonmonotonic feature with respect to  $W$  in the behavior of the correlation function  $C(l, t)$  in the interacting case. Still, we have made a notable observation that  $t_0$  corresponds to the time  $t$  when the behavior of the correlation function changes qualitatively, i.e., from a strongly nonequilibrium-type behavior ( $t < t_0$ ) to that of a steady-state type ( $t > t_0$ ). Once  $t$  exceeds  $t_c$ , the correlation function  $C(l, t)$  tends to become time independent, indicating that the quantum state  $|\Psi(t)\rangle$  reaches a steady state. This observation suggests that  $S_{\max}$  is a good quantity that encodes the transition or crossover of the system or of the state  $|\Psi(t)\rangle$  from a nonequilibrium to a steady state.

## VII. CONCLUDING REMARKS

In this paper, we have highlighted the differences in the dynamical behavior between non-Hermitian and Hermitian disordered systems based on the quasiparticle picture. First, we have systematically studied the dynamical behavior of the many-body HN model, including  $n_j(t)$ ,  $n_k(t)$ , and  $S_{\text{ent}}$ , using the Krylov subspace method. Although the difference between non-Hermitian and Hermitian systems is somewhat masked in the behavior of  $n_j(t)$  in real space, we find that it sharply manifest in  $n_k(t)$ , and in  $S_{\text{ent}}$  as well. In the noninteracting system, we demonstrated both numerically and analytically the characteristic relaxation of  $n_k(t)$ , where  $n_k(t)$  converges either to 0 (for  $k > 0$ ) or to 1 (for  $k < 0$ ) in the clean limit. This behavior stems from the presence of  $\text{Im}(E)$ , which is an intrinsic nature of the non-Hermitian system. We also discussed the relationship between the relaxation of  $n_k(t)$

<sup>8</sup>We note that we can also use  $S_{\text{ent}}(\infty)$  as a quantity to characterize the delocalization-localization transition. We expect that  $S_{\text{ent}}(\infty)$  obeys the volume law in the delocalized phase and the area law in the delocalized phase, reflecting the property of  $|\alpha_1\rangle$ .



and  $S_{\text{ent}}$  based on the quasiparticle picture and provided an intuitive explanation for the nonmonotonic behavior of  $S_{\text{ent}}$  as a function of  $W$ . Interestingly, we found that  $S_{\text{ent}}$  exhibits a nonmonotonic behavior as a function of time in the interacting case. By carefully examining the distribution of  $\text{Im}(E)$ , especially, through comparison with the noninteracting, we have clarified the nature of this nonmonotonic time evolution, which is unique to this non-Hermitian interacting system.

The nonmonotonic behavior of  $S_{\text{ent}}$  with respect to time stems from  $\text{Im}(E)$ , which implies the instability of the many-body localized phase [109,110]. Recent studies suggest that thermalization symptoms [111,112] appear even in a strongly disordered system, resulting in the study of many-body delocalization-localization transition [113–117] at a turning point. They have examined the response of a quantum system to the inclusion of thermal grain [118] and evaluated the imaginary part of eigenenergy [119], which may relate to the real-complex transition of the HN model.

For the noninteracting case, we have recently noticed that the nonmonotonic behavior of  $S_{\text{ent}}(t \rightarrow \infty)$  is also reported in Ref. [108]. They have employed a recently proposed numerical approach [120] instead of the exact diagonalization and performed calculations in larger system sizes compared to ours. Their findings indicate that the scaling of  $S_{\text{ent}}(t \rightarrow \infty)$  exhibits logarithmic area-law transition. This result is in contradiction with our findings at critical regime ( $W \sim W_c$ ), which may come from the finite-size effect. This discrepancy raises a new question as to whether  $S_{\text{ent}}$  obeys volume-law scaling in an interacting system. We intend to address this question in future work.

### ACKNOWLEDGMENTS

QUSPIN [121,122] has been employed for generating the matrix elements of Eq. (1). K.-I.I. thanks M. Schiro and K. Kawabata for useful discussions, comments, and suggestions. This work was supported by JSPS KAKENHI Grants No. JP23KJ0360 (T.O.), No. JP20K03788, and No. JP21H01005 (K.-I.I.), and JST SPRING: Grant No. JPMJSP2132 (T.O.).

### APPENDIX A: A VIEWPOINT FROM THE LINDBLAD/GKSL EQUATION

The Lindblad/GKSL equation [73,74] is a fundamental equation describing a quantum system coupled to an environment or a measuring apparatus. The GKSL equation is expressed as

$$\frac{\partial \rho(t)}{\partial t} = -i[H_{\text{eff}}, \rho(t)] + \sum_m L_m \rho(t) L_m^\dagger, \quad (\text{A1})$$

where  $H_{\text{eff}} = H - \frac{i}{2} \sum_m L_m^\dagger L_m$ , and  $L_m$  is called the Lindblad operator that stems from the interaction between the original quantum system and environment or a measuring apparatus.

The purpose of this Appendix is to clarify the relationship between Eq. (A1) and Eqs. (10) and (13). Indeed, Eqs. (10) and (13) can be derived from Eq. (A1) by simply neglecting the second term of Eq. (A1). Without the second term, the evolution of the density matrix  $\rho(t)$  is determined by an effective von Neumann equation prescribed by the generally non-Hermitian effective Hamiltonian  $H_{\text{eff}}$ . If a pure state is

chosen as an initial state, this dynamics coincides with the one obtained in the time evolution so that  $|\Psi(t)\rangle$  is determined by Eqs. (10) and (13). Conversely, our non-Hermitian Schrödinger dynamics prescribed by Eqs. (10) and (13) may be thus justified in the context of the GKSL description of an open quantum system.

Of course, why and under what circumstances the second term of Eq. (A1) is negligible is left to be explained (one may need also a further justification), and so is the meaning of neglecting the second term. This may be best illustrated in the so-called quantum trajectory picture [123] (cf. also quantum jump [124] and first-order Monte Carlo methods [125,126]). In this picture the time evolution of a wave function  $|\Psi(t)\rangle$  is regarded as a stochastic process described below, and a series of such a stochastic process (corresponding to the entire time evolution of the wave function) is referred to as a quantum trajectory; in the end, an ensemble average of many trajectories will be taken. Also, here, the environment means an ensemble of measuring apparatus, represented by an operator  $L_m$ . After each time step of  $\delta t$ , a quantum state  $|\Psi(t)\rangle$  evolves with a probability  $1 - p$  into

$$|\Psi(t + \delta t)\rangle = \frac{(1 - iH_{\text{eff}}\delta t)|\Psi(t)\rangle}{\sqrt{1 - p}} \quad (\text{A2})$$

and with a probability  $p_m$  into

$$|\Psi(t + \delta t)\rangle = \frac{L_m |\Psi(t)\rangle}{\sqrt{p_m/\delta t}}, \quad (\text{A3})$$

where  $p = \sum_m p_m$  and  $p_m = \langle \Psi(t) | L_m^\dagger L_m | \Psi(t) \rangle \delta t$ . Equation (A3) describes the case in which the measurement apparatus  $m$  obtains an outcome, while Eq. (A2) describes the situation in which none of the measurement apparatus obtains an outcome, i.e., the case of null outcome. A series of this stochastic process determines a single trajectory of the quantum state  $|\Psi(t)\rangle$ . Our non-Hermitian Schrödinger dynamics prescribed by Eqs. (10) and (13) is, on the other hand, obtained by selecting, after each time step, the case of null outcome (postselection) or, in other words, by projecting the quantum state onto its subspace of such successive null outcomes (or by choosing such a trajectory). Note that in Eq. (A2) a change in the amplitude of the wave function in the numerator, i.e.,  $(1 - iH_{\text{eff}}\delta t)|\Psi(t)\rangle$ , is precisely compensated by the normalization factor  $\sqrt{1 - p}$  in the denominator, which is equivalent to the renormalization we adopted in Eq. (13).

### APPENDIX B: OTHER DEFINITIONS OF THE ENTANGLEMENT ENTROPY

Since a non-Hermitian system has right and left eigenvectors, three possible definitions of  $S_{\text{ent}}$  and density matrix  $\Omega$  have been considered. In particular,  $S_{\text{ent}}$  is defined as

$$S_{\text{ent}}^{R,R} = -\text{Tr}[\rho_{R,R} \ln(\rho_{R,R})], \quad (\text{B1})$$

$$S_{\text{ent}}^{L,L} = -\text{Tr}[\rho_{L,L} \ln(\rho_{L,L})], \quad (\text{B2})$$

and

$$S_{\text{ent}}^{R,L} = -\text{Tr}[\rho_{R,L} \ln(\rho_{R,L})], \quad (\text{B3})$$

where  $\rho_{R,R} = \text{Tr}_B[|\alpha\rangle\langle\alpha|/\langle\alpha|\alpha\rangle]$ ,  $\rho_{L,L} = \text{Tr}_B[|\alpha\rangle\rangle\langle\langle\alpha|/\langle\langle\alpha|\alpha\rangle\rangle]$ , and  $\rho_{R,L} = \text{Tr}_B[|\alpha\rangle\langle\langle\alpha|/\langle\langle\alpha|\alpha\rangle\rangle]$ . Here, a superscript

( $R$  or  $L$ ) represents which eigenstate (left or right) is used to construct the density matrix. The definition we employ in this work relates to Eq. (B1), which yields a non-negative value of  $S_{\text{ent}}$  as well as  $S_{\text{ent}}$  of a Hermitian system. This non-negativity of  $S_{\text{ent}}$  holds, which can be shown by Schmid value decomposition. Whereas, in the case of Eq. (B3), the non-negativity of  $S_{\text{ent}}$  does not have to hold since  $\rho_{R,L}$  can become a non-Hermitian matrix, which has been studied in the context of nonunitary conformal field theory (CFT) [127,128]. Furthermore, in this case, the qualitative behavior of Rényi entropy does not coincide with  $S_{\text{ent}}$  [129], which is hardly seen in the Hermitian case and in Eqs. (B1) and (B2) [130]. The previous study mainly focused on the static behavior (eigenvector) of Eq. (B3) and, thus, it may be an interesting direction to investigate the dynamical behavior of Eq. (B3).

### APPENDIX C: CHOICE OF THE BOUNDARY CONDITIONS: EFFECT OF THE SKIN EFFECT

The Hatano-Nelson model exhibits a so-called non-Hermitian skin effect under the open boundary conditions (OBC). Skin effect is a localization phenomenon where an extensive number of the eigenstates are at the boundary with real eigenenergy. Although this feature has already been reported in the original works of Hatano and Nelson, it has now been recognized as a hallmark of topological phases of non-Hermitian physics. Here, we comment on whether or how the choice of OBC (skin effect) affects features of entanglement dynamics compared to our study [periodic boundary condition (PBC)]. In the quench dynamics under OBC, the nonreciprocal hopping makes the density dynamics asymmetrical in motion, which is also observed in the case of PBC, but the density is to be eventually localized at the boundary reflecting OBC. Reference [120] has demonstrated many-body HN model under OBC in the clean limit exhibits entanglement transition due to skin effect. They have reported that entanglement entropy obeys logarithmic scaling, which is the same as the case of periodic boundary conditions. However, the effective central charge is not equal to one. They have analyzed this entanglement transition and shown that it originates from the skin effect. Recently, both Refs. [108,131] have investigated how disorder potential affects this entanglement transition. Interestingly, they have reported that entanglement entropy exhibits nonmonotonic behavior as a function of disorder strength in the case of OBC as well as that of PBC. In the delocalized phase, entanglement entropy increases with the increase in disorder strength. However, in the localized phase, entanglement entropy decreases with the increase in disorder strength. While the origin of suppression of entanglement in the case of OBC is different from that of PBC, we consider that the quasiparticle picture and our discussion is still useful. In the case of OBC, quasiparticle corresponds to skin mode, which is robust and localized at the boundary even if backscattering occurs. However, as the disorder strength increases, the quasiparticle (skin mode) tends to move bidirectional rather than unidirectional motion due to backscattering as well as that of PBC, resulting in an increase in entanglement entropy. Thus, disorder dependence of entanglement entropy is qualitatively independent of the choice of the boundary condition.

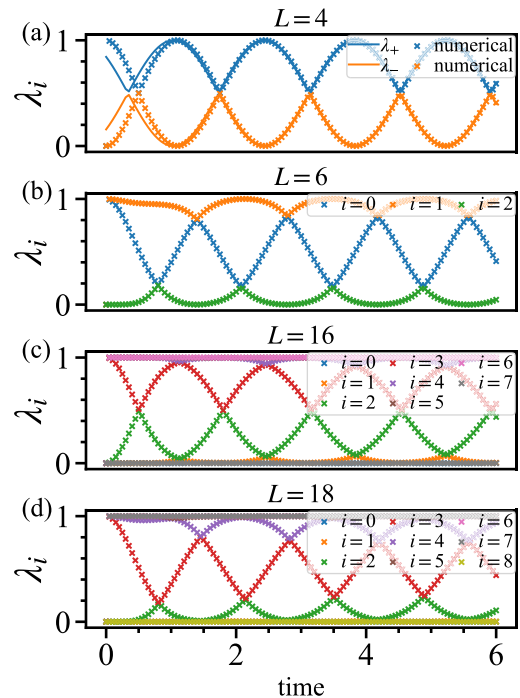


FIG. 11. Time evolution of the eigenvalues  $\lambda_k$  of correlation function (D4): (a)  $L = 4$ , (b)  $L = 6$ , (c)  $L = 16$ , and (d)  $L = 18$ . In (a), solid lines  $\lambda_{\pm} = \frac{1}{2} \pm \frac{1}{2} \sqrt{\frac{1}{2} [\sin[4 \cosh(g)t + \phi] + 1]}$  are analytical solutions, where  $\phi$  is a fitting parameter.  $g = 0.5$ .

### APPENDIX D: ORIGIN OF THE OSCILLATORY BEHAVIOR OF $S_{\text{ent}}$ IN THE WEAKLY DISORDERED REGIME

Let us focus on the behavior of  $S_{\text{ent}}(t)$  in the weakly disordered regime depicted in Fig. 4. We have noticed that a small rapid oscillation is conspicuous on top of its global tendency to saturate. The oscillation is also rather conspicuous in the noninteracting case [Fig. 4(a)], and in the case of even number of particles  $L/2 = 6, 8, 10$ . Here, we show that the oscillation stems from a twofold degeneracy (in the imaginary part) of the asymptotic state.

To simplify the argument, let us consider here the noninteracting case, in which  $S_{\text{ent}}$  is simply given by the eigenvalues  $\lambda_i$  of the correlation function in the subsystem (of size  $\ell = L/2$ ) [89]

$$\mathbf{C} = \begin{pmatrix} \langle c_1^\dagger c_1 \rangle & \dots & \langle c_1^\dagger c_\ell \rangle \\ \vdots & \ddots & \vdots \\ \langle c_\ell^\dagger c_1 \rangle & \dots & \langle c_\ell^\dagger c_\ell \rangle \end{pmatrix}, \quad (\text{D1})$$

as

$$S_{\text{ent}} = - \sum_{i=1}^{i=L/2} [\lambda_i \ln(\lambda_i) + (1 - \lambda_i) \ln(1 - \lambda_i)]. \quad (\text{D2})$$

The four panels of Fig. 11 show the behavior of numerically evaluated  $\lambda_i$ 's in the cases of different number of particles  $L/2$ . The plots show that there exists a qualitative difference in the behavior of  $\lambda_i$ 's between the cases of  $L/2$  even and odd; in the case of  $L/2$  even, a pair of  $\lambda_i$ 's appear symmetrically

with respect to  $\lambda = \frac{1}{2}$ , while in the case of  $L/2$  odd, there exists no such pairwise behavior. Since  $\lambda_i$ 's taking a value close to  $\lambda = \frac{1}{2}$  gives the most relevant contribution to  $S_{\text{ent}}$ , one naturally expects that such a pairwise behavior of  $\lambda_i$ 's in the case of  $L/2$  even leads to a conspicuous oscillation of  $S_{\text{ent}}$  in this case.

The reason why  $S_{\text{ent}}$  is oscillatory in the first place may be understood in the following way. In the asymptotic time regime  $t \rightarrow \infty$  only the following two many-body states with with a maximal imaginary part in the eigenenergy are relevant:

$$|\Psi(t \rightarrow \infty)\rangle = \frac{1}{\sqrt{2}}(e^{-i\epsilon_k = -\pi t} c_{k=-\pi}^\dagger + e^{-i\epsilon_k = 0t} c_{k=0}^\dagger) \times \prod_{k=-2\pi/L}^{k=-2\pi/L \times (L/2-1)} e^{-i\epsilon_k t} c_k^\dagger |0\rangle. \quad (\text{D3})$$

One can estimate the the correlation function (D3) in this asymptotic regime as

$$\begin{aligned} C_{n,m} &= \left[ \frac{1}{L} \sum e^{ik(n-m)} \right] + \frac{1}{2L} (e^{-i\pi(n-m)} + 1) \\ &+ \frac{1}{2L} (-1)^{L/2} (e^{-4i \cosh(g)t} e^{i\pi n} + e^{4i \cosh(g)t} e^{-i\pi m}). \end{aligned} \quad (\text{D4})$$

This matrix can be easily diagonalized, e.g., in case of  $L = 4$ . In Fig. 11(a) the analytic value of  $\lambda_i$ 's thus obtained are compared with the ones found numerically. The plots show that in most of the time regime considered in the figure except the very early one around  $t \simeq 0$  the two plots coincide, indicating that the system is indeed controlled by the asymptotic state (D3), and the twofold degeneracy (in the imaginary part) of the two relevant eigenstates is the origin of the fast oscillation of  $S_{\text{ent}}$  in this case.

#### APPENDIX E: NOTES ON THE GENERALIZED GIBBS ENSEMBLE

In the limit of  $t \rightarrow \infty$ ,  $t_c(k) < t$  for all  $k$  are satisfied, and then  $|\Psi(t)\rangle$  reaches an equilibrium state. Generally, we can obtain the corresponding statistical ensemble, assuming principle of maximum entropy under some constraint, such as expectation values of energy or total particles, using Lagrange multipliers. In case of integrable systems, our target ( $W = 0$  and  $V = 0$ ) realized statistical ensemble is called generalized Gibbs ensemble (GGE), which forms maximum entropy under the constraint of  $\hat{n}_k$ . GGE is defined as

$$\rho_{\text{GGE}} \equiv \frac{e^{-\sum_k \lambda_k \hat{n}_k}}{Z}, \quad (\text{E1})$$

where  $Z = \text{Tr}[e^{-\sum_k \lambda_k \hat{n}_k}]$ , and  $\lambda_k$  is the Lagrange multiplier that imposes constraint  $\langle \Psi(t=0) | \hat{n}_k | \Psi(t=0) \rangle = \langle \Psi(\infty) | \hat{n}_k | \Psi(\infty) \rangle$ . GGE describes the expectation value of various quantities as well as the saturation value of  $S_{\text{ent}}$ . The statistical expectation value of  $\hat{n}_k$  is defined by

$$\begin{aligned} \langle \hat{n}_k \rangle_{\text{GGE}} &\equiv \text{Tr}(\rho_{\text{GGE}} \hat{n}_k) = -\frac{\partial}{\partial \lambda_k} \log(Z) \\ &= \frac{1}{1 + \exp(\lambda_k)} = \langle \Psi(t) | \hat{n}_k | \Psi(t) \rangle. \end{aligned} \quad (\text{E2})$$

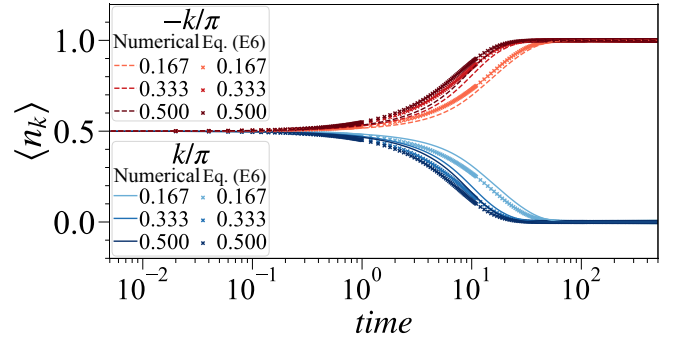


FIG. 12. Time evolution of  $\langle \hat{n}_k \rangle$ :  $L = 12$ ,  $W = 0$ , and  $V = 0$ . The numerical result is obtained by averaging over 100 different initial states [Eq. (F1)]. Both solid and dashed lines represent numerical result, while a scatter plot represents Eq. (E6).

Additionally, the thermodynamic entropy of GGE is in accordance with the saturation value of  $S_{\text{ent}}$  in the thermodynamic limit, i.e.,

$$\begin{aligned} S_{\text{ent}}(\infty) &= \lim_{L \rightarrow \infty} S_{\text{thermo}} \\ &\equiv \lim_{L \rightarrow \infty} -\text{Tr} \rho_{\text{GGE}} \ln \rho_{\text{GGE}} \\ &= \lim_{L \rightarrow \infty} \sum s_k \equiv \ell \int dk s(k). \end{aligned} \quad (\text{E3})$$

$S_{\text{ent}}(\infty)$  follows a volume law [ $S_{\text{ent}}(\infty) \propto \ell$ ] if most  $\langle \hat{n}_k \rangle$  take neither 0 or 1, which is consistent to the fact that thermal entropy obeys volume law.

In the Hermitian case, since  $\hat{n}_k$  is a conserved quantity,  $\langle \Psi(t) | \hat{n}_k | \Psi(t) \rangle$  remains constant value over time, while  $\langle \Psi(t) | \hat{n}_k | \Psi(t) \rangle$  varies during dynamics in the case of the many-body HN model due to the nonunitary time evolution  $\partial_t \langle \hat{n}_k \rangle = i \langle \Psi(t) | H^\dagger \hat{n}_k - \hat{n}_k H | \Psi(t) \rangle \neq 0$ . Let us focus on the relaxation of  $\langle \Psi(t) | \hat{n}_k | \Psi(t) \rangle$ , which is naively formulated by

$$\begin{aligned} \langle \hat{n}_k \rangle &= \frac{\langle \Psi(0) | e^{iH^\dagger t} \hat{n}_k e^{-iHt} | \Psi(0) \rangle}{\langle \Psi(0) | e^{iH^\dagger t} e^{-iHt} | \Psi(0) \rangle} \\ &= \frac{\text{Tr}(|\Psi_{\{k\}}\rangle^2 \hat{n}_k e^{2 \sum_k \text{Im}(\epsilon_k) \hat{n}_k t})}{\text{Tr}(|\Psi_{\{k\}}\rangle^2 e^{2 \sum_k \text{Im}(\epsilon_k) \hat{n}_k t})}, \end{aligned} \quad (\text{E4})$$

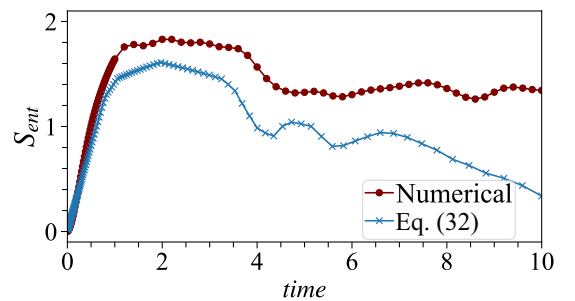


FIG. 13. Time evolution of  $S_{\text{ent}}$  (red solid line with circles) and the quasiparticle picture [Eq. (32), blue solid line with crosses]:  $L = 16$ ,  $W = 0$ , and  $V = 0$ . We choose the DW state as the initial state. We take into account the possibility of quasiparticles moving from the left (or right) end to the opposite end in the calculation (32) (for more details, refer to Ref. [86]).

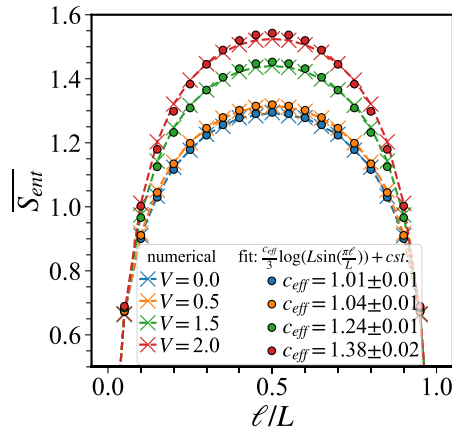


FIG. 14. Scaling of  $S_{\text{ent}}$  as a function of  $\ell/L$  with various values of  $V$ :  $L = 20$  and  $W = 0$ . A dashed line represents a numerical result, while a scatter plot represents a fitting curve.

where  $\epsilon_k$  is a single-particle eigenenergy (see Supplemental Material [43]) and  $\Psi_{\{k\}} = \langle \{n_k\} | \Psi(0) \rangle = \langle n_{k_1} \dots n_{k_L} | \Psi(0) \rangle$ ;  $|\{n_k\}\rangle$  represents the Fock space in momentum space. Here, we assume  $|\Psi_{\{k\}}|^2$  is expressed as a GGE, so that

$$\begin{aligned} \langle \hat{n}_k \rangle &= \frac{\text{Tr}(|\Psi_{\{k\}}|^2 \hat{n}_k e^{2 \sum_k \text{Im}(\epsilon_k) \hat{n}_k t})}{\text{Tr}(|\Psi_{\{k\}}|^2 e^{2 \sum_k \text{Im}(\epsilon_k) \hat{n}_k t})} \\ &\sim \frac{\text{Tr}(\hat{n}_k e^{\sum_k [-\lambda_k + 2 \text{Im}(\epsilon_k) t] \hat{n}_k})}{Z}, \end{aligned} \quad (\text{E5})$$

where  $Z = \text{Tr}(e^{\sum_k [-\lambda_k + 2 \text{Im}(\epsilon_k) t] \hat{n}_k})$ , and we assume superposition consists of various filling to use the knowledge of the grand canonical ensemble. We can derive time-dependent behavior of  $\langle \hat{n}_k \rangle$ , which is defined as

$$\begin{aligned} \langle \hat{n}_k \rangle &= \frac{\text{Tr}(\hat{n}_k e^{\sum_k [-\lambda_k + 2 \text{Im}(\epsilon_k) t] \hat{n}_k})}{Z} \\ &= -\frac{\partial}{\partial \{[\lambda_k - 2 \text{Im}(\epsilon_k) t]\}} \log(Z) \\ &= \frac{1}{1 + e^{-2 \text{Im}(\epsilon_k) t}}, \end{aligned} \quad (\text{E6})$$

where in the last line we take all  $\lambda_k$  to be 0, which is justified in case the initial state is prepared as DW state. Equation (E6) implies that an imaginary eigenenergy either amplifies or decays a corresponding mode  $\langle \hat{n}_k \rangle$  and this relaxation depends on the magnitude of  $\text{Im}(\epsilon_k)$ .

#### APPENDIX F: TIME DEPENDENCE OF $\langle \hat{n}_k \rangle$ FOR FREE-PARTICLE CASE

In Sec. IV, we observed  $\langle \hat{n}_k \rangle$  converge to stationary values more rapidly than Eq. (E6). This discrepancy appears to arise from the fact that we assume  $Q = \sum_i k_i$  takes the

values ranging from 0 to  $L$  to derive an analytical expression of  $\langle \hat{n}_k \rangle$ , although we employ half-filling sector in actual numerical calculation. To justify Eq. (E6), we select the initial state as

$$|\Psi(0)\rangle = \sum_{Q=0}^{Q=L} \frac{1}{\sqrt{L+1}} |\{n_k^Q\}\rangle, \quad (\text{F1})$$

where  $|\{n_k^Q\}\rangle$  is the Fock state that satisfies with  $\sum_i k_i = Q$  and we randomly choose the Fock state  $|\{n_k^Q\}\rangle$ . Figure 12 shows the time evolution of  $\langle \hat{n}_k \rangle$  with the initial state given in Eq. (F1). The behavior of  $\langle \hat{n}_k \rangle$  is closer to Eq. (E6) than the result shown in Fig. 5.

#### APPENDIX G: QUASIPARTICLE PICTURE FOR NONRECIPROCAL SYSTEM

In the HN model, quasiparticles decay or amplify under time evolution, leading to the question of when the quasiparticle picture becomes ill defined. To address this question, we compare numerical results with the result suggested by the quasiparticle picture, as shown in Fig 13. Initially, the result suggested by the quasiparticle picture agrees with the numerical result; however, as time evolves, it begins to converge to 0, which differs from the numerical result. This discrepancy stems from the assumption within the quasiparticle picture that  $S_{\text{ent}}$  behaves as thermal entropy, whereas in this case,  $S_{\text{ent}}$  actually characterizes quantum correlation. Additionally, this discrepancy contrasts with a recent study in which the quasiparticle picture is used to describe the entanglement dynamics in the non-Hermitian system ( $PT$ -symmetric system) [25]. As quasiparticles exhibit unidirectional motion in the HN model, the question of whether the quasiparticle picture quantitatively still describes entanglement dynamics is intriguing. The quasiparticle picture can be compatible and generalized to many physical situations, such as an inhomogeneous initial state [132] and a state with no quasiparticle pair structure [133]. Therefore, further study is necessary to generalize the quasiparticle picture to the HN model, which may become a framework for non-Hermitian GGE.

#### APPENDIX H: THE EFFECT OF INTERACTION ON THE SCALING OF $S_{\text{ent}}(\infty)$

Figure 14 shows the saturation value of  $S_{\text{ent}}$  as a function  $\ell/L$  with various values of  $V$ . For weak  $V$ , a discrepancy between a numerical result (dashed line) and a fitting function (scatter plot), which is a form of Eq. (38), is negligible, but it becomes more noticeable for large  $V$ . Although a finite discrepancy exists for large  $V$ , a fitting function [Eq. (38)] qualitatively characterizes numerical results, leading us to conclude that the scaling of  $S_{\text{ent}}$  is logarithmic.

[1] A. Einstein, B. Podolsky, and N. Rosen, *Phys. Rev.* **47**, 777 (1935).

[2] S. J. Freedman and J. F. Clauser, *Phys. Rev. Lett.* **28**, 938 (1972).



- [3] J.-W. Pan, D. Bouwmeester, H. Weinfurter, and A. Zeilinger, *Phys. Rev. Lett.* **80**, 3891 (1998).
- [4] A. Aspect, *Phys. Rev. D* **14**, 1944 (1976).
- [5] A. Aspect, J. Dalibard, and G. Roger, *Phys. Rev. Lett.* **49**, 1804 (1982).
- [6] A. Aspect, P. Grangier, and G. Roger, *Phys. Rev. Lett.* **49**, 91 (1982).
- [7] J. M. Deutsch, *Phys. Rev. A* **43**, 2046 (1991).
- [8] M. Srednicki, *Phys. Rev. E* **50**, 888 (1994).
- [9] M. Rigol, V. Dunjko, and M. Olshanii, *Nature (London)* **452**, 854 (2008).
- [10] M. Rigol, V. Dunjko, V. Yurovsky, and M. Olshanii, *Phys. Rev. Lett.* **98**, 050405 (2007).
- [11] M. Rigol, A. Muramatsu, and M. Olshanii, *Phys. Rev. A* **74**, 053616 (2006).
- [12] A. Iucci and M. A. Cazalilla, *Phys. Rev. A* **80**, 063619 (2009).
- [13] L. Vidmar and M. Rigol, *J. Stat. Mech.: Theory Exp.* (2016) 064007.
- [14] P. Calabrese and J. Cardy, *J. Stat. Mech.: Theory Exp.* (2005) P04010.
- [15] V. Alba and P. Calabrese, *Proc. Natl. Acad. Sci. USA* **114**, 7947 (2017).
- [16] M. Fagotti and P. Calabrese, *Phys. Rev. A* **78**, 010306(R) (2008).
- [17] G. D. Chiara, S. Montangero, P. Calabrese, and R. Fazio, *J. Stat. Mech.: Theory Exp.* (2006) P03001.
- [18] P. Calabrese, *Phys. A (Amsterdam)* **504**, 31 (2018), lecture Notes of the 14th International Summer School on Fundamental Problems in Statistical Physics.
- [19] R. Nandkishore and D. A. Huse, *Annu. Rev. Condens. Matter Phys.* **6**, 15 (2015).
- [20] D. A. Abanin, E. Altman, I. Bloch, and M. Serbyn, *Rev. Mod. Phys.* **91**, 021001 (2019).
- [21] D. N. Page, *Phys. Rev. Lett.* **71**, 1291 (1993).
- [22] X. Turkeshi and M. Schirò, *Phys. Rev. B* **107**, L020403 (2023).
- [23] B. Skinner, J. Ruhman, and A. Nahum, *Phys. Rev. X* **9**, 031009 (2019).
- [24] Y. Fuji and Y. Ashida, *Phys. Rev. B* **102**, 054302 (2020).
- [25] A. Bácsi and B. Dóra, *Phys. Rev. B* **103**, 085137 (2021).
- [26] Y. L. Gal, X. Turkeshi, and M. Schirò, *SciPost Phys.* **14**, 138 (2023).
- [27] Y. Li, X. Chen, and M. P. A. Fisher, *Phys. Rev. B* **100**, 134306 (2019).
- [28] A. Chan, R. M. Nandkishore, M. Pretko, and G. Smith, *Phys. Rev. B* **99**, 224307 (2019).
- [29] S. Choi, Y. Bao, X.-L. Qi, and E. Altman, *Phys. Rev. Lett.* **125**, 030505 (2020).
- [30] A. Zabalo, M. J. Gullans, J. H. Wilson, S. Gopalakrishnan, D. A. Huse, and J. H. Pixley, *Phys. Rev. B* **101**, 060301(R) (2020).
- [31] X. Turkeshi, R. Fazio, and M. Dalmonte, *Phys. Rev. B* **102**, 014315 (2020).
- [32] S. Sang and T. H. Hsieh, *Phys. Rev. Res.* **3**, 023200 (2021).
- [33] Z. Yang, D. Mao, and C.-M. Jian, *Phys. Rev. B* **108**, 165120 (2023).
- [34] C. Noel, P. Niroula, D. Zhu, A. Risinger, L. Egan, D. Biswas, M. Cetina, A. V. Gorshkov, M. J. Gullans, D. A. Huse, and C. Monroe, *Nat. Phys.* **18**, 760 (2022).
- [35] J. M. Koh, S.-N. Sun, M. Motta, and A. J. Minnich, *Nat. Phys.*, **19**, 1314 (2023).
- [36] R. Vasseur, A. C. Potter, Y.-Z. You, and A. W. W. Ludwig, *Phys. Rev. B* **100**, 134203 (2019).
- [37] M. J. Gullans and D. A. Huse, *Phys. Rev. X* **10**, 041020 (2020).
- [38] Y. Kuno, T. Orito, and I. Ichinose, *Phys. Rev. B* **106**, 214304 (2022).
- [39] N. Hatano and D. R. Nelson, *Phys. Rev. B* **56**, 8651 (1997).
- [40] N. Hatano and D. R. Nelson, *Phys. Rev. B* **58**, 8384 (1998).
- [41] N. Hatano and D. R. Nelson, *Phys. Rev. Lett.* **77**, 570 (1996).
- [42] S. Longhi, *Phys. Rev. B* **103**, 054203 (2021).
- [43] See Supplemental Material at <http://link.aps.org/supplemental/10.1103/PhysRevB.108.214308> for a numerical demonstration and detailed explanation of wave-packet dynamics. The Supplemental Material also contains Refs. [134–136].
- [44] T. Orito and K.-I. Imura, *Phys. Rev. B* **105**, 024303 (2022).
- [45] Y. Saad, *SIAM J. Numer. Anal.* **29**, 209 (1992).
- [46] S. Aubry and G. André, *Ann. Israel Phys. Soc.* **3**, 133 (1980).
- [47] Z. Gong, Y. Ashida, K. Kawabata, K. Takasan, S. Higashikawa, and M. Ueda, *Phys. Rev. X* **8**, 031079 (2018).
- [48] S. Yao and Z. Wang, *Phys. Rev. Lett.* **121**, 086803 (2018).
- [49] K. Yokomizo and S. Murakami, *Phys. Rev. Lett.* **123**, 066404 (2019).
- [50] K.-I. Imura and Y. Takane, *Phys. Rev. B* **100**, 165430 (2019).
- [51] K.-I. Imura and Y. Takane, *Prog. Theor. Exp. Phys.* **2020**, 12A103 (2020).
- [52] Y. Ashida, Z. Gong, and M. Ueda, *Adv. Phys.* **69**, 249 (2020).
- [53] T. Yoshida and Y. Hatsugai, *Phys. Rev. B* **106**, 205147 (2022).
- [54] K. Kawabata, K. Shiozaki, and S. Ryu, *Phys. Rev. B* **105**, 165137 (2022).
- [55] S.-B. Zhang, M. M. Denner, T. c. v. Bzdusek, M. A. Sentef, and T. Neupert, *Phys. Rev. B* **106**, L121102 (2022).
- [56] A. Banerjee, R. Sarkar, S. Dey, and A. Narayan, *J. Phys.: Condens. Matter* **35**, 333001 (2023).
- [57] T. Yoshida and Y. Hatsugai, *Phys. Rev. B* **107**, 075118 (2023).
- [58] P. Molignini, O. Arandes, and E. J. Bergholtz, *Phys. Rev. Res.* **5**, 033058 (2023).
- [59] R. Qi, J. Cao, and X.-P. Jiang, *arXiv:2306.03807*.
- [60] L.-J. Zhai, G.-Y. Huang, and S. Yin, *Phys. Rev. B* **106**, 014204 (2022).
- [61] K. Suthar, Y.-C. Wang, Y.-P. Huang, H. H. Jen, and J.-S. You, *Phys. Rev. B* **106**, 064208 (2022).
- [62] J. Liu and Z. Xu, *Phys. Rev. B* **108**, 184205 (2023).
- [63] L.-J. Zhai, S. Yin, and G.-Y. Huang, *Phys. Rev. B* **102**, 064206 (2020).
- [64] J.-Q. Cheng, S. Yin, and D.-X. Yao, *arXiv:2307.08750*.
- [65] J. Mák, M. J. Bhaseen, and A. Pal, *arXiv:2301.01763*.
- [66] K. Slevin and T. Ohtsuki, *Phys. Rev. Lett.* **82**, 382 (1999).
- [67] K. Slevin and T. Ohtsuki, *New J. Phys.* **16**, 015012 (2014).
- [68] K. Kawabata and S. Ryu, *Phys. Rev. Lett.* **126**, 166801 (2021).
- [69] X. Luo, T. Ohtsuki, and R. Shindou, *Phys. Rev. B* **104**, 104203 (2021).
- [70] S. Heußen, C. D. White, and G. Refael, *Phys. Rev. B* **103**, 064201 (2021).
- [71] A. Panda and S. Banerjee, *Phys. Rev. B* **101**, 184201 (2020).
- [72] D. C. Brody, *J. Phys. A: Math. Theor.* **47**, 035305 (2014).
- [73] G. Lindblad, *Commun. Math. Phys.* **48**, 119 (1976).
- [74] V. Gorini, A. Kossakowski, and E. C. G. Sudarshan, *J. Math. Phys.* **17**, 821 (1976).
- [75] R. Hamazaki, K. Kawabata, and M. Ueda, *Phys. Rev. Lett.* **123**, 090603 (2019).

- [76] Y. Qin and L. Li, [arXiv:2307.07964](https://arxiv.org/abs/2307.07964).
- [77] M. Žnidarič, T. c. v. Prosen, and P. Prelovšek, *Phys. Rev. B* **77**, 064426 (2008).
- [78] J. H. Bardarson, F. Pollmann, and J. E. Moore, *Phys. Rev. Lett.* **109**, 017202 (2012).
- [79] M. Serbyn, Z. Papić, and D. A. Abanin, *Phys. Rev. Lett.* **110**, 260601 (2013).
- [80] M. Serbyn, Z. Papić, and D. A. Abanin, *Phys. Rev. Lett.* **111**, 127201 (2013).
- [81] D. A. Huse, R. Nandkishore, and V. Oganesyan, *Phys. Rev. B* **90**, 174202 (2014).
- [82] D. J. Luitz, N. Laflorencie, and F. Alet, *Phys. Rev. B* **93**, 060201(R) (2016).
- [83] E. V. H. Doggen, F. Schindler, K. S. Tikhonov, A. D. Mirlin, T. Neupert, D. G. Polyakov, and I. V. Gornyi, *Phys. Rev. B* **98**, 174202 (2018).
- [84] P. P. Mazza, J.-M. Stéphan, E. Canovi, V. Alba, M. Brockmann, and M. Haque, *J. Stat. Mech.: Theory Exp.* (2016) 013104.
- [85] A. Avella and F. Mancini, *Strongly Correlated Systems: Numerical Methods*, Springer Series in Solid-State Sciences (Springer, Berlin, 2013).
- [86] R. Modak, V. Alba, and P. Calabrese, *J. Stat. Mech.: Theory Exp.* (2020) 083110.
- [87] T. Orito and K.-I. Imura, *Proceedings of the 29th International Conference on Low Temperature Physics (LT29)* (IEEE, Piscataway, NJ, 2023), Vol. 38 p. 011187.
- [88] P. Calabrese and J. Cardy, *J. Phys. A: Math. Theor.* **42**, 504005 (2009).
- [89] I. Peschel, *J. Phys. A: Math. Gen.* **36**, L205 (2003).
- [90] P. Calabrese and J. Cardy, *J. Stat. Mech.: Theory Exp.* (2004) P06002.
- [91] C. Holzhey, F. Larsen, and F. Wilczek, *Nucl. Phys. B* **424**, 443 (1994).
- [92] G. Vidal, J. I. Latorre, E. Rico, and A. Kitaev, *Phys. Rev. Lett.* **90**, 227902 (2003).
- [93] S. Furukawa, V. Pasquier, and J. Shiraishi, *Phys. Rev. Lett.* **102**, 170602 (2009).
- [94] M. E. Fisher and R. E. Hartwig, *Adv. Chem. Phys.* **15**, 333 (1969).
- [95] B.-Q. Jin and V. E. Korepin, *J. Stat. Phys.* **116**, 79 (2004).
- [96] S. Nishimoto, *Phys. Rev. B* **84**, 195108 (2011).
- [97] L. Mao, Y. Hao, and L. Pan, *Phys. Rev. A* **107**, 043315 (2023).
- [98] Y. Ishiguro, J. Sato, and K. Nishinari, *Phys. Rev. Res.* **5**, 033102 (2023).
- [99] K. Yamamoto, M. Nakagawa, M. Tezuka, M. Ueda, and N. Kawakami, *Phys. Rev. B* **105**, 205125 (2022).
- [100] S. R. White, *Phys. Rev. Lett.* **69**, 2863 (1992).
- [101] U. Schollwöck, *Ann. Phys.* **326**, 96 (2011).
- [102] T. Orito, Y. Kuno, and I. Ichinose, *Phys. Rev. B* **103**, L060301 (2021).
- [103] P. Sierant and J. Zakrzewski, *Phys. Rev. B* **105**, 224203 (2022).
- [104] R. Blankenbecler, D. J. Scalapino, and R. L. Sugar, *Phys. Rev. D* **24**, 2278 (1981).
- [105] S. Duane, A. Kennedy, B. J. Pendleton, and D. Roweth, *Phys. Lett. B* **195**, 216 (1987).
- [106] T. Hayata and A. Yamamoto, *Phys. Rev. B* **104**, 125102 (2021).
- [107] S.-X. Hu, Y. Fu, and Y. Zhang, *Phys. Rev. B* **108**, 245114 (2023).
- [108] K. Li, Z.-C. Liu, and Y. Xu, [arXiv:2305.12342](https://arxiv.org/abs/2305.12342).
- [109] W. De Roeck and F. Huvneers, *Phys. Rev. B* **95**, 155129 (2017).
- [110] T. Thiery, F. Huvneers, M. Müller, and W. De Roeck, *Phys. Rev. Lett.* **121**, 140601 (2018).
- [111] M. Kiefer-Emmanouilidis, R. Unanyan, M. Fleischhauer, and J. Sirker, *Phys. Rev. Lett.* **124**, 243601 (2020).
- [112] F. Evers and S. Bera, The internal clock of many-body (de-)localization, *Phys. Rev. B* **108**, 134204 (2023).
- [113] N. Macé, F. Alet, and N. Laflorencie, *Phys. Rev. Lett.* **123**, 180601 (2019).
- [114] N. Laflorencie, G. Lemarié, and N. Macé, *Phys. Rev. Res.* **2**, 042033(R) (2020).
- [115] S. Roy and D. E. Logan, *Phys. Rev. B* **101**, 134202 (2020).
- [116] G. De Tomasi, I. M. Khaymovich, F. Pollmann, and S. Warzel, *Phys. Rev. B* **104**, 024202 (2021).
- [117] M. S. Bahovadinov, W. Buijsman, A. K. Fedorov, V. Gritsev, and D. V. Kurlov, *Phys. Rev. B* **106**, 224205 (2022).
- [118] A. Morningstar, D. A. Huse, and J. Z. Imbrie, *Phys. Rev. B* **102**, 125134 (2020).
- [119] A. Morningstar, L. Colmenarez, V. Khemani, D. J. Luitz, and D. A. Huse, *Phys. Rev. B* **105**, 174205 (2022).
- [120] K. Kawabata, T. Numasawa, and S. Ryu, *Phys. Rev. X* **13**, 021007 (2023).
- [121] P. Weinberg and M. Bukov, *SciPost Phys.* **2**, 003 (2017).
- [122] P. Weinberg and M. Bukov, *SciPost Phys.* **7**, 20 (2019).
- [123] A. J. Daley, *Adv. Phys.* **63**, 77 (2014).
- [124] M. B. Plenio and P. L. Knight, *Rev. Mod. Phys.* **70**, 101 (1998).
- [125] J. Dalibard, Y. Castin, and K. Mølmer, *Phys. Rev. Lett.* **68**, 580 (1992).
- [126] R. Dum, P. Zoller, and H. Ritsch, *Phys. Rev. A* **45**, 4879 (1992).
- [127] D. Bianchini, O. A. Castro-Alvaredo, and B. Doyon, *Nucl. Phys. B* **896**, 835 (2015).
- [128] R. Couvreur, J. L. Jacobsen, and H. Saleur, *Phys. Rev. Lett.* **119**, 040601 (2017).
- [129] Y.-T. Tu, Y.-C. Tzeng, and P.-Y. Chang, *SciPost Phys.* **12**, 194 (2022).
- [130] K. D. Agarwal, T. K. Konar, L. G. C. Lakkaraju, and A. S. De, [arXiv:2305.08374](https://arxiv.org/abs/2305.08374).
- [131] S.-Z. Li, X.-J. Yu, and Z. Li, [arXiv:2309.03546](https://arxiv.org/abs/2309.03546).
- [132] V. Alba, *Phys. Rev. B* **97**, 245135 (2018).
- [133] B. Bertini, E. Tartaglia, and P. Calabrese, *J. Stat. Mech.: Theory Exp.* (2018) 063104.
- [134] T. Eichelkraut, R. Heilmann, S. Weimann, S. Stützer, F. Dreisow, D. N. Christodoulides, S. Nolte, and A. Szameit, *Nat. Commun.* **4**, 2533 (2013).
- [135] S. Longhi, *Phys. Rev. Res.* **1**, 023013 (2019).
- [136] D. J. Thouless, *Phys. Rev. B* **28**, 4272 (1983).